A Novel Thermally Stable Segmented Solid Paraboloid Antenna for High Surface Accuracy

H Li*, Q Li† and Z Wu‡
School of Mechanical Engineering and Mechanics, Ningbo University, Ningbo, 315211, People's Republic of China.

The rapidly growing communication demands in our society require the design of high-performance solid paraboloid antennas with extremely high surface accuracy, which remains a challenge due to the inevitable thermal deformations. In this study, we proposed a novel design of thermally stable segmented solid surface antenna with high surface accuracy. In this novel design, the antenna reflector is divided into a certain number of segmented pieces, each of which is then individually supported by an innovative Thermally Stable Grid Structure (TSGS). An analytical model based on Sanders improved first-approximation shell theory is developed to predict the thermal deformation of antenna surface, with which the proposed segmenting method in improving the surface accuracy of reflector antenna is theoretically approved. The working mechanism of the proposed TSGS that the thermal deformations at the supporting points can maintain a minimum level is verified using finite element analysis. A case study is performed in a practical environment to demonstrate that a segmented antenna supported by TSGS can largely suppress the thermal deformation compared with a continuous surface antenna. This study provides a novel and useful engineering solution for paraboloid solid surface antennas to achieve extremely high surface accuracy under various thermal conditions.

Nomenclature

A	=	matrix of in-plane stiffness (A_{ij}), N/m
A_1, A_2	=	Lamé parameters of the parabolic revolution surface
c_1, c_2	=	constants resulting from integration
E_{11}, E_{22}	=	Young's modulus, Pa
f	=	focal length of an antenna, m
G_{12}	=	shear modulus, Pa
k	=	Gaussian curvature

*Senior Researcher, School of Mechanical Engineering and Mechanics, Ningbo University
†Researcher, School of Mechanical Engineering and Mechanics, Ningbo University
‡Corresponding Author, School of Mechanical Engineering and Mechanics, Ningbo University (nbuwu309@126.com)

N	=	in-plane resultant forces (N_{ij}), N/m
$\bar{Q}$	=	transformed stiffness coefficients ($\bar{Q}_{mn}$)
R_1, R_2	=	radii of principal curvatures of the parabolic revolution surface
U, V, W	=	displacements along x, y and z axes, respectively, in a Cartesian coordinate system, m
u, v, w	=	displacements along the local curvilinear coordinates and
	=	the normal direction of the parabolic revolution surface, respectively, m
x, y, z	=	axes in a Cartesian coordinate system
α	=	equivalent thermal expansion coefficients (α_{ij})
δ	=	angle between the normal of the revolution surface and
	=	the axisymmetric axis (one local curvilinear coordinate), rad
θ	=	angle between the meridian plane and the Cartesian coordinate plane xz
	=	(one local curvilinear coordinate), rad
κ	=	bending and twisting curvature (κ_{ij})
μ	=	Poisson's ratio
ξ_1, ξ_2	=	general variables for curvilinear coordinates
$\varepsilon_{11}, \varepsilon_{22}, \gamma_{12}$	=	mid-plane strains
ϑ	=	ply-angle, rad

I. Introduction

The increasing use of frequency bands by communications drives both qualitative and quantitative demands of high performance and high precision antennas in recent years [1–3]. High-precision antennas have been received wide applications in satellites such as remote sensing, meteorology, communications, telemetry or radio astronomy [1, 4, 5].

Up to date, many forms of antennas have been put forward. In general, the antennas can be categorized into three types, i.e. solid surface antennas, inflatable antennas and cable-net antennas [6]. In recent years, the mesh and inflatable antennas attracted lots of research interests due to their small storage volume [7, 8]. A milestone in development of inflatable antennas is a $14m$-diameter and $2.0 \times 1.1 \times 0.46m^3$ folded volume inflatable antenna proposed in 1996 [9]. Europe also developed a large-aperture inflatable antenna with $12m$ diameter [10, 11]. However, the inflatable antennas have relatively poor surface precision, due to the thermal deformation, gas leakage and etc. [6]. In the past decades, many forms of cable-net antennas with different types of supported structure have been developed, manufactured and tested, such as wrapped rib antenna, radial rib antenna, hoop column antenna, and hoop truss antenna, etc. [12–15]. Among these cable-net antennas, the hoop truss antennas have attracted lots of attentions and research interests in last two decades [16, 17], and also have been applied in practical communication satellites [18, 19]. The surface accuracy of

a mesh antenna is often better than that of a inflatable antenna, however, the mesh antennas are mainly used in L-band because of their millimeter–level surface accuracy. With the development of antenna structure, the mesh antennas with much higher surface accuracy have been achieved. On the other hand, the solid surface antennas remain to be a preferable technical solution for data transmission of satellites. This is because the solid surface antennas can provide many favorable advantages, such as high surface accuracy, high directivity, high radiation efficiency, low side lobe levels and permanent working capacity [8, 20, 21].

The change of working environment during the operation period of satellites will inevitably result in the deformation or even distortion to antenna surface due to various thermal conditions [2]. The temperature of an antenna severely varies due to different working scenarios. The thermal deformation of the antenna reflector in turn can cause serious issues, such as a distorted far-field radiation pattern, shift of the aiming point and the increase of the antenna side lobes etc. [2]. These deleterious effects will eventually cause signals distorted and even incorrect information to be received or sent [1, 2]. Therefore, accurate prediction of the thermal deformation of the antenna surface and largely suppressing the thermal effects are of critical importance for the design of high-precision antennas. In general, for a well-designed antenna reflector, the Root Mean Square (RMS) surface error should achieve the precision in a range of $0.02\lambda \sim 0.03\lambda$, where λ represents the wave length [1]. As the working frequency of antennas rapidly grows in communication applications in the last decade, the high shape stability and surface accuracy against the temperature variation is a critical design requirement for antennas. The suppression of thermal deformations of antennas now is a major technical challenge to accomplish a high-precision solid surface antenna.

To suppress the thermal effects for a solid surface antenna, a direct method is to apply the materials with low thermal expansion coefficients as the main structural components. Therefore, carbon fiber reinforced polymer (CFRP) composite materials are widely used on antennas, as the thermal expansion coefficients of CFRP materials are much low compared with that of metal materials [3, 22, 23]. Theoretically, a zero equivalent thermal expansion coefficient can be achieved for CFRP materials if the composite lay-up is well designed. However, unexpected out-of-plane thermal deformation of CFRP antennas can be easily generated due to the fiber orientation errors, the moisture absorption effects or the other uncertainty factors [23, 24]. Recently, the active control method has been proposed to correct the low-order, thermally-induced distortions of the antenna using piezoelectric actuators [25]. It is experimentally demonstrated that the method of using piezoelectric actuator is an effective means for correcting the thermal distortion at a level of $10\mu m$ [25]. However, the major disadvantage of an active control system is that a high precision measuring system is needed, simultaneously, to monitor the thermal deformation of the antenna. However, active structural elements often cause mismatch of the coefficients of thermal expansion (CTE) in the structure. This CTE mismatch may result in even larger thermal distortion to the reflectors than that of the conventional designs without using active elements. As a consequence, the reduced system reliability and the high costs of resources make the active control system become unacceptable for the thermal deformation control of satellite antennas.

As the active control method is too costly, a passive method becomes a preferable choice for suppressing the thermal effects of an antenna working in space. In view of the fact that the thermal deformation of the antenna is unavoidable due to the limitation of available materials, a novel concept for designing thermally stable antennas with high surface accuracy is proposed in this study. Instead of directly making efforts to suppress the thermal strains of antenna surface to zero, we reduce the thermal RMS surface error of the antenna reflector through segmenting the antenna reflector into a certain number of pieces. Segmenting a solid surface antenna into pieces is not a completely new concept, for example the Precision Segmented Reflector (PSR) proposed in 1990s [26–28]. The aim of this PSR project was to develop the technology of large aperture solid surface space antenna for future advanced astrophysics missions [29]. Due to the large aperture, in this PSR design, the antenna reflector was assembled by a number of segments. The PSR project mainly concentrated on the development of deployable back support truss structure of the reflector [29, 30], design of the reflector panel [27], manufacturing methods and materials etc [26, 30]. The segmented antenna now is a widely accepted method for developing large aperture antenna. However, most of the previous research and working efforts mainly concentrated on the manufacturing accuracy for the reflector panels [26, 27] and the active adjusting method [31]. None of these research works studied the functionality of applying a segmenting design method for the solid antennas to achieve high surface accuracy under various thermal conditions.

In this study, we will demonstrate, both theoretically and numerically, that the surface error of a solid surface antenna under thermal loadings can be reduced, dramatically, by segmenting the reflector surface into pieces. To this end, an analytical model based on Sanders improved first-approximation thin shell theory [32] is developed to predict the RMS surface error of either continuous or segmented antenna reflectors. The mechanism of reducing the thermal surface error through segmenting the reflector surface is discussed and verified by a parametric study of the RMS surface error of segmented antenna reflectors with respect to the number of segment sections. Subsequently, an innovative design of Thermally Stable Grid Structure (TSGS) is proposed to support each segmented panel of the antenna reflector. The principle of this TSGS mechanism is based on an innovative design of an irregular-hexagon structural cell, in which the thermal displacements of CFRP walls along one direction (defined as x) can be compensated by means of the thermal expansion or shrink of an internal aluminum web at the other direction (defined as y). As a consequence, the induced thermal stresses and deformations of the whole structure have negligible influence to the positions of mounting (supporting) points. From simulation results, it approves that applying this thermally stable grid structure to segmented antenna reflector can achieve negligible RMS surface error during temperature variations. At the end of this paper, the surface accuracy of the novel segmented antenna reflector is predicted under different working scenarios, and the prediction results are compared with that of continuous antenna reflectors.

II. Theoretical Model

In this section, an analytical model is developed to predict the thermal deformation of a composite solid surface paraboloid antenna under uniformly distributed thermal loading. In a Cartesian coordinate system, the thin shell of revolution for a paraboloid antenna is defined as,

$$z = \frac{1}{4f}(x^2 + y^2) \tag{1}$$

where f denotes the focal length of an antenna. The paraboloid antenna is modeled as an axisymmetric shell structure, the kinematic equations of which are defined under an axisymmetric coordinate system, as illustrated in Fig. 1-a. At any point on the surface of this parabolic shell of revolution, we can define two principal sections on the revolution surface of the shell, which then creates two plane curves with two local principal radii of curvatures R_1 and R_2 [33], respectively, as shown in Fig. 1-b. Analogous to the earth, one plane curve is called *the meridional curve* and the projection of another curve on the plane perpendicular to the axis of the parabolic shell is *the parallel circle*. With these two curves, the angle δ is defined to represent the angle between the normal of the revolution surface and the axisymmetric axis, and the angle θ is defined between *the meridian plane* and the Cartesian coordinate plane xz, as shown in Fig. 1-b. The position of any point on the surface can be determined using these two angle parameters. Therefore, angles δ and θ are used to define as the curvilinear coordinates in the modelling. If we analogize this curvilinear coordinate to a Geographic coordinate system (GCS), the physical meaning of these two angles can be interpreted as, δ defines the position of a latitude line, whilst θ is the degree of a meridian (longitude line).

Based on Sanders improved first-approximation theory with considering the curvilinear coordinates $\xi_1 = \delta$ and $\xi_2 = \theta$, the kinematic equations and the equilibrium equations of a paraboloid antenna take the following forms as [32, 34],

$$\begin{aligned}
\varepsilon_{11} &= \frac{1}{A_1}\frac{\partial u}{\partial \delta} + \frac{1}{A_1 A_2}\frac{\partial A_1}{\partial \theta}v + \frac{w}{R_1} \\
\varepsilon_{22} &= \frac{1}{A_2}\frac{\partial v}{\partial \theta} + \frac{1}{A_1 A_2}\frac{\partial A_2}{\partial \delta}u + \frac{w}{R_2} \\
\gamma_{12} &= \frac{A_2}{A_1}\frac{\partial}{\partial \delta}\left(\frac{v}{A_2}\right) + \frac{A_1}{A_2}\frac{\partial}{\partial \theta}\left(\frac{u}{A_1}\right) \\
k_{11} &= -\frac{1}{A_1}\frac{\partial}{\partial \delta}\left(\frac{1}{A_1}\frac{\partial w}{\partial \delta} - \frac{u}{R_1}\right) - \frac{1}{A_1 A_2}\left(\frac{1}{A_2}\frac{\partial w}{\partial \theta} - \frac{v}{R_2}\right)\frac{\partial A_1}{\partial \theta} \\
k_{22} &= -\frac{1}{A_2}\frac{\partial}{\partial \theta}\left(\frac{1}{A_2}\frac{\partial w}{\partial \theta} - \frac{v}{R_2}\right) - \frac{1}{A_1 A_2}\left(\frac{1}{A_1}\frac{\partial w}{\partial \delta} - \frac{u}{R_1}\right)\frac{\partial A_2}{\partial \delta} \\
k_{12} &= -\frac{A_2}{A_1}\frac{\partial}{\partial \delta}\left[\frac{1}{A_2}\left(\frac{1}{A_2}\frac{\partial w}{\partial \theta} - \frac{v}{R_2}\right)\right] - \frac{A_1}{A_2}\frac{\partial}{\partial \theta}\left[\frac{1}{A_1}\left(\frac{1}{A_1}\frac{\partial w}{\partial \delta} - \frac{u}{R_1}\right)\right] \\
&\quad + \frac{1}{2A_1 A_2}\left(\frac{1}{R_2} - \frac{1}{R_1}\right)\left[\frac{\partial (A_2 v)}{\partial \delta} - \frac{\partial (A_1 u)}{\partial \theta}\right]
\end{aligned} \tag{2a}$$

$$
\begin{aligned}
&\frac{\partial(A_2N_{11})}{\partial\delta}+\frac{\partial(A_1N_{12})}{\partial\theta}+\frac{\partial A_1}{\partial\theta}N_{12}-\frac{\partial A_2}{\partial\delta}N_{22}+\frac{A_1A_2}{R_1}Q_1\\
&+\frac{A_1}{2}\frac{\partial}{\partial\theta}\left[\left(\frac{1}{R_1}-\frac{1}{R_2}\right)M_{12}\right]=0\\
&\frac{\partial(A_2N_{12})}{\partial\delta}+\frac{\partial(A_1N_{22})}{\partial\theta}+\frac{\partial A_2}{\partial\theta}N_{12}-\frac{\partial A_1}{\partial\delta}N_{11}+\frac{A_1A_2}{R_2}Q_2\\
&+\frac{A_2}{2}\frac{\partial}{\partial\delta}\left[\left(\frac{1}{R_2}-\frac{1}{R_1}\right)M_{12}\right]=0\\
&\frac{\partial(A_2Q_1)}{\partial\delta}+\frac{\partial(A_1Q_2)}{\partial\theta}-A_1A_2\left(\frac{N_{11}}{R_1}+\frac{N_{22}}{R_2}\right)=0\\
&\frac{\partial(A_2M_{11})}{\partial\delta}+\frac{\partial(A_1M_{12})}{\partial\theta}+\frac{\partial A_1}{\partial\theta}M_{12}-\frac{\partial A_2}{\partial\delta}M_{22}-A_1A_2Q_1=0\\
&\frac{\partial(A_2M_{12})}{\partial\delta}+\frac{\partial(A_1M_{22})}{\partial\theta}+\frac{\partial A_2}{\partial\delta}M_{12}-\frac{\partial A_1}{\partial\theta}M_{11}-A_1A_2Q_2=0
\end{aligned}
\tag{2b}
$$

where ε_{ij} and k_{ij} (i,j=1,2) denote the strain and the curvature variation, respectively. $N_{ij}(i,j=1,2)$ are membrane resultant forces, and $M_{ij}(i,j=1,2)$ are bending moment. Q_1, Q_2 are transverse stress resultants. A_1 and A_2 are Lamé parameters. u, v and w are the displacements along the local curvilinear coordinates ($\xi_1=\delta, \xi_2=\theta$) and the normal direction (m) of the parabolic revolution surface of antenna, respectively. R_1 and R_2 are the radii of principal curvatures, as shown in Fig. 1-b. For a thin parabolic shell of revolution, Lamé coefficients and radii of principal curvatures are derived as,

$$
\begin{aligned}
A_1&=\frac{2f}{\cos^3(\delta)}, \quad A_2=2f\tan(\delta)\\
R_1&=\frac{2f}{\cos^3(\delta)}, \quad R_2=\frac{2f}{\cos(\delta)}
\end{aligned}
\tag{3}
$$

Note, in the derivation of Eq. (3), the curvature equation $k=\frac{z''}{(1+(z')^2)^{3/2}}$ rather than its approximation form $k=z''$ must be used.

In this study, the antenna reflector is constructed by sandwich composite curved panels with Aluminum honeycomb core. The thickness of the antenna reflector is relatively small compared with the radii of principal curvatures of the reflector, therefore, it can be modelled as a thin shell structure. A symmetric and balanced lay-up for the sandwich composite shell typically denoted by $[\pm\vartheta/\mp\vartheta/\text{core}/\pm\vartheta/\mp\vartheta]$ is applied, in which ϑ is the lay-up angle of unidirectional fiber reinforced composite ply with respect to the meridional curve of the antenna reflector. A paraboloid antenna, which is mounted at the vertex and under a uniformly distributed temperature loading is in axisymmetric membrane state. As a result, the curvature variations of the membrane equal to zero. The displacements u, v and w and the Lamé coefficients A_1 and A_2 merely depend on the first coordinate parameter δ. Thus, the kinematic functions of the paraboloid antenna

reflector of Eq. (2b) can be further simplified as,

$$\begin{aligned}
\varepsilon_{11} &= \frac{1}{A_1}\frac{du}{d\delta} + \frac{w}{R_1} \\
\varepsilon_{22} &= \frac{1}{A_1 A_2}\frac{dA_2}{d\delta}u + \frac{w}{R_2} \\
\gamma_{12} &= \frac{A_2}{A_1}\frac{d}{d\delta}\left(\frac{v}{A_2}\right) \\
k_{11} &= k_{22} = k_{12} = 0
\end{aligned} \tag{4}$$

Based on the thin shell theory (Love 1927, [35]), applying the Kirchhoff-Love hypothesis and assuming that the stress along the thickness direction is negligible, the constitution equation of the antenna shell is expressed as,

$$\begin{bmatrix} \sigma_{11}^i \\ \sigma_{22}^i \\ \sigma_{12}^i \end{bmatrix} = \begin{bmatrix} \overline{Q}_{11}^i & \overline{Q}_{12}^i & \overline{Q}_{16}^i \\ \overline{Q}_{21}^i & \overline{Q}_{22}^i & \overline{Q}_{26}^i \\ \overline{Q}_{16}^i & \overline{Q}_{26}^i & \overline{Q}_{66}^i \end{bmatrix} \begin{bmatrix} \varepsilon_{11} - \overline{\alpha}_{11}^i \Delta T \\ \varepsilon_{22} - \overline{\alpha}_{22}^i \Delta T \\ \gamma_{12} - \overline{\alpha}_{12}^i \Delta T \end{bmatrix} \tag{5}$$

where the superscript ^{i} denotes the i-th ply, $\overline{Q}_{mn}^i$ and $\overline{\alpha}_{mn}^i$ (m,n=1,2) are the transformed stiffness coefficients and the thermal expansion coefficients, respectively. Integrating the stresses along the shell thickness, the in-plane resultant forces for the composite shell with symmetric lay-ups take the following form,

$$\begin{bmatrix} N_{11} \\ N_{22} \\ N_{12} \end{bmatrix} = \begin{bmatrix} A_{11} & A_{12} & A_{16} \\ A_{12} & A_{22} & A_{26} \\ A_{16} & A_{26} & A_{66} \end{bmatrix} \begin{bmatrix} \varepsilon_{11} - \alpha_{11}\Delta T \\ \varepsilon_{22} - \alpha_{22}\Delta T \\ \gamma_{12} - \alpha_{12}\Delta T \end{bmatrix} \tag{6}$$

where N_{ij} $(i, j = 1, 2)$ are the in-plane resultant forces, A_{ij} $(i, j = 1, 2, 6)$ are the stretching stiffness of composite laminates, α_{ij} are equivalent thermal expansion coefficients. The derivation of α_{ij} is presented in Appendix-II. Eqs. (4), (5) and (6) indicate that, the in-plane resultant forces N_{ij} are merely the functions of δ. Thus, for a thin shell reflector antenna in axisymmetric membrane state, the equilibrium equations (2b) of the paraboloid antenna reflector then can be simplified as,

$$\begin{aligned}
\frac{dA_2 N_{11}}{d\delta} - \frac{dA_2}{d\delta}N_{22} &= 0 \\
\frac{dA_2 N_{12}}{d\delta} + \frac{dA_2}{d\delta}N_{12} &= 0 \\
\frac{N_{11}}{R_1} + \frac{N_{22}}{R_2} &= 0
\end{aligned} \tag{7}$$

The three unknown variables given by Eqs. (7) are determinable with analytical solutions, which are $N_{ij} = c \times e^{\int_{ij}(\delta)}$ with an unknown coefficient c. At the edge of this antenna reflector, the resultant forces $N_{12} = N_{11} = 0$, which indicate that the unknown parameters c in the expressions of N_{ij} also equals to zero. Thus, $N_{ij} = 0$ (i,j=1,2). According to Eq. (6), the following expressions are obtained,

$$\begin{aligned} \varepsilon_{11} &= \alpha_{11}\Delta T \\ \varepsilon_{22} &= \alpha_{22}\Delta T \\ \gamma_{12} &= \alpha_{12}\Delta T \end{aligned} \tag{8}$$

Substituting Eq. (8) into Eq. (5) and making some necessary simplification, the following governing equations for a membrane state antenna reflector under a uniformly distributed temperature loading are obtained as,

$$\begin{aligned} \frac{1}{A_1}\frac{du}{d\delta} + \frac{w}{R_1} &= \alpha_{11}\Delta T \\ \frac{1}{A_1 A_2}\frac{dA_2}{d\delta}u + \frac{w}{R_2} &= \alpha_{22}\Delta T \\ \frac{A_2}{A_1}\frac{d}{d\delta}\left(\frac{v}{A_2}\right) &= \alpha_{12}\Delta T \end{aligned} \tag{9}$$

Substituting the expressions of Lamé coefficients and radii of principal curvatures in Eq. (3), and combining the first two equations to eliminate the variable w, we can arrive,

$$\begin{aligned} &\frac{\cos^3\delta}{2f}\frac{du}{d\delta} - \left(\frac{\cos^3\delta}{2f}\cot\delta\right)u - \alpha_{11}\Delta T + \alpha_{22}\Delta T\cos^2\delta = 0 \\ &\frac{\sin\delta}{\cos^2\delta}\frac{d}{d\delta}\left(\frac{\cos^3\delta}{2f}v\right) - \alpha_{12}\Delta T = 0 \\ &w - \frac{2f}{\cos^3\delta}\alpha_{11}\Delta T + \frac{du}{d\delta} = 0 \end{aligned} \tag{10}$$

where u and v can be obtained from the first two equations, and the displacements w can be determined by u. As this is an axisymmetric problem with respect to geometry, loading and boundary conditions, the displacements u, v, w are independent of θ. The general solution of Eq. (10) can be expressed as,

$$\begin{aligned} u(\delta) &= \alpha_{11}\Delta T\, f\, \sin\delta\sec^2\delta + 2f\Delta T\,(\alpha_{11}-\alpha_{22})\ln(\tan\delta)\sin\delta + c_1\sin\delta \\ v(\delta) &= 2f\Delta T\alpha_{12}\left[\ln(\tan\delta/2) + \sec\delta\right]\tan\delta + 2c_2 f\tan(\delta) \\ w(\delta) &= -c_1\cos(\delta) - 2f(\alpha_{11}-\alpha_{22})\Delta T\,(\cos\delta\ln(\tan\delta) + \sec\delta) + f\alpha_{11}\Delta T\sec\delta \end{aligned} \tag{11}$$

In Eq. (11), c_1 and c_2 are unknown coefficients. If the antenna is mounted at its vertex, the unknown coefficient c_1 can be determined from the boundary conditions, namely, $w(0) = 0$. However, the term $\ln\tan(\delta)$ in Eq. (11) will

give rise to a singularity when $\delta = 0$. To avoid this singularity, we impose an artificial boundary condition to the antenna instead of directly applying the vertex mounting constraint, as $w(0.01)\cos(0.01) - u(0.01)\sin(0.01) = 0$, which indicates that the displacement component of the circle $\delta = 0.01$ along the z axis (vertical direction) of Cartesian coordinate system equates to zero. Note, this modified boundary condition is only used to simulate a similar constraint with the vertex mounting boundary condition of $w(0) = 0$, and has barely influence to the simulation results on the thermal deformation of the antenna. On the other hand, this singularity also exists in the FEM simulation, for which the axisymmetric meshes with a further refinement around the vertex must be applied to achieve the convergent results. However, the mesh quality has no influence on the results of composite layup with 45-degree ply-angle (as presented in Figs. 14-15, 20-21), because this singularity is not existed at the vertex of the antenna for the case of 45-degree ply-angle. The composite layup with 45-degree ply-angle has equivalent thermal expansion coefficients $\alpha_{11} = \alpha_{22}$, which leads to the elimination of all the singularity terms $\ln\tan\delta$ in the analytical model.

After applying the modified boundary condition, $w(0.01)\cos(0.01) - u(0.01)\sin(0.01) = 0$, the coefficient c_1 in Eq. (11) is derived as,

$$c_1 \approx f\Delta T\alpha_{11}\left(1 - 2\frac{(\alpha_{11} - \alpha_{22})}{\alpha_{11}}\left[\ln\tan(0.01)\right] + 1\right) \tag{12}$$

For a continuous surface antenna with symmetric and balanced composite lay-ups under a membrane state, the equivalent thermal coefficient $\alpha_{12} = 0$, and $v(0) = 0$, from which the other unknown coefficient c_2 is determined, as $c_2 = 0$.

Equation (11) indicates that the thermal deformations of a composite paraboloid antenna reflector with symmetric lay-ups only depend on the thermal expansion coefficients and the focal length. Therefore, for minimizing the thermal deformations of antenna reflector, the key is to decrease the thermal expansion coefficients. Eq. (11) highlights the potential advantages of applying composite materials for the design of antenna reflector, as the equivalent thermal expansion coefficients of which can be suppressed through the optimization of lay-ups. In addition to the ply angles, the thermal expansion coefficients of composite can be affected by many other factors, such as the material properties of carbon fiber and matrix, the volume ratios of carbon fiber and matrix, and the ply thickness etc. However, zero equivalent thermal expansion coefficients hardly can be achieved for practical composite materials. In this study, instead of seeking for such structural materials with extremely low thermal expansion coefficients, we focus on the study of applying the proposed segmenting method to achieve high surface precision for a paraboloid antenna. Obviously, the surface accuracy of the antenna reflector can be further improved if we apply this segmenting method and low thermal expansion structural materials, simultaneously.

The analytical solutions of the thermal displacements predicted by Eq. (11), i.e. $\sqrt{u^2(\delta) + w^2(\delta)}$, are obtained and used to compare with the results given by the finite element analysis (FEA), for the purpose of verification, as shown in Fig. 2. The material properties of the sandwich composite shell for the antenna reflector are listed in Table. 1. The composite properties used in this study are given by CFRP T700/5428, which is manufactured using the standard

prepreg/autoclave process. T700 denotes the type of carbon fiber (with a high tensile strength around 700 ksi) and 5428 indicates the type of bismaleimide resin. The composite type of T700/5428 is selected in this work because T700/5428 has been widely used in industrial/commercial applications and it has stable mechanical performance in high temperature environment. The antenna reflector is modeled using the commercial finite element analysis software Abaqus with shell elements S4R. A uniform temperature field of 0° is applied on the model of antenna reflector, and is elevated in a subsequent "static" analysis step. The analytical solution of thermal deformation predicted by Eq. (11) coincide well with FEA results.

Table 1 Material properties of sandwich composite shell

Aluminum honeycomb core	$E_{11} = 8 \times 10^4$ Pa, $E_{22} = 8 \times 10^4$ Pa, $G_{12} = 1.5 \times 10^4$ Pa, $\mu_{12} = 0.33$, $\alpha_1^\circ = 20 \times 10^{-6}/°\text{C}$, $\alpha_2^\circ = 20 \times 10^{-6}/°\text{C}$, $\alpha_{12}^\circ = 0 \times 10^{-6}/°\text{C}$, thickness = 20 mm
Composite laminates	$E_{11} = 145$ GPa, $E_{22} = 9$ GPa, $G_{12} = 5.69$ GPa, $\mu_{12} = 0.312$, $\alpha_1^o = -0.5 \times 10^{-6}/°\text{C}$, $\alpha_2^o = 25 \times 10^{-6}/°\text{C}$, $\alpha_{12}^\circ = 0 \times 10^{-6}/°\text{C}$, thickness = 0.1 mm
Aluminum	$E = 70$ GPa, $\mu = 0.3$, $\alpha^\circ = 23 \times 10^{-6}/°\text{C}$

In a Cartesian coordinate system, the displacements of any a point on the antenna mid-surface take the following form as,

$$\begin{aligned} U(x,y) &= (u(\delta)\cos(\delta) + w(\delta)\sin(\delta))\cos(\theta) - v(\delta)\sin(\theta) \\ V(x,y) &= (u(\delta)\cos(\delta) + w(\delta)\sin(\delta))\sin(\theta) + v(\delta)\cos(\theta) \\ W(x,y) &= -w(\delta)\cos\delta + u(\delta)\sin(\delta) \end{aligned} \tag{13}$$

where $U(x,y)$, $V(x,y)$ and $W(x,y)$ denote the displacements along x, y and z axes, respectively. The relationships between the curvilinear coordinates (δ, θ) and the Cartesian coordinates (x, y, z) are given by,

$$\delta = \tan^{-1}\left[\frac{\sqrt{x^2+y^2}}{2f}\right], \ \theta = \tan^{-1}\left(\frac{y}{x}\right) \tag{14}$$

In this paper, a two-step procedure method is applied to accurately evaluate the surface accuracy of a paraboloid antenna reflector under a thermal loading [33]. Firstly, a new paraboloid surface is fitted according to the displacements evaluated by Eq. (13) and the original surface of the antenna reflector given by Eq. (1). Secondly, the Root Mean Square (RMS) value of the surface error between the deformed antenna mid-surface and the new fitted paraboloid surface is calculated, which is termed as RMS$[\Delta_i]$ hereinafter. A full derivation process for this evaluation method of

RMS[Δ_i] is presented in Appendix-I.

Under a uniformly temperature thermal loading, the values of RMS[Δ_i] of the paraboloid antenna reflectors with different fiber angles ϑ in the composite lay-up are predicted and presented in Fig. 3. For this case, the RMS[Δ_i] of the paraboloid antenna reflector with the fiber angle of 45° gives a minimum value, which is 145 μm. Fig. 3 also indicates that the values of RMS[Δ_i] is sensitive to the fiber angle ϑ. If the ϑ has an error of $+1°$ or $-1°$, the value of RMS[Δ_i] increases to 652 μm and 371 μm, respectively. This implies that an uncertainty analysis may be necessary for the prediction of the surface accuracy RMS[Δ_i] of antenna reflector, however, this is out of the research scope of this paper.

III. The Segmented Paraboloid Antenna Reflector

The parametric study in the above section indicates that, for a continuous paraboloid antenna reflector, minimizing the equivalent thermal expansion coefficients of the composite shell is the most direct and effective means to improve the surface accuracy, i.e., lowering the RMS[Δ_i]. However, in practical, the equivalent thermal expansion coefficients of composite materials can hardly achieve zero [24, 36]. Consequently, instead of lowering the thermal expansion coefficients, in this study we propose another design concept to suppress the value of RMS[Δ_i] and achieve high-precision reflector, i.e. segmenting the antenna reflector into a certain number of separate parts.

For example, as illustrated in Fig. 4, an antenna reflector is segmented symmetrically into 6 pieces, each of which is mounted at its own geometric center for the antenna reflector. The segmented antenna reflectors remain in a membrane state under a uniform temperature thermal loading, and the internal stress state is identical with that of a continuous surface antenna reflector mounted at its vertex. For each piece of an individual segmented reflector, the displacement fields u, v, and w are also derived in a similar way as the last section. We assume that u and w are independent with θ, while v depends on both δ and θ due to the segmenting. Note, in the analysis of segmented reflector, the angle θ herein indicates a local rotation angle θ for each segmented piece. For the case of 6 segmented pieces shown in Fig. 4, the angle θ is in the range of $[-30° \leq \theta \leq 30°]$ for each piece, whilst the angle θ is $[0° \leq \theta \leq 360°]$ for a continuous antenna reflector. The expressions for u, v and w are obtained by solving Eq.(10). Note, without losing much accuracy, we assumed that v is linearly varying with respect to the angle θ from Eq. (9) as,

$$v(\delta, \theta) = A_2 \int \frac{A_1}{A_2} \alpha_{12} \Delta T d\delta + A_2 c_2 \theta \tag{15}$$

where c_2 is an unknown coefficient. Substituting Eq. (15) into Eq. (10), the displacement fields for each segment u, v,

and w are obtained to take the following form as,

$$\begin{aligned} u(\delta) &= \alpha_{11}\Delta T f \sin(\delta)\sec(\delta)^2 + 2f\left(\Delta T\alpha_{11} - \Delta T\alpha_{22} + c_2\right)\ln\tan(\delta)\sin(\delta) + c_1\sin(\delta) \\ v(\delta,\theta) &= 2f\Delta T\alpha_{12}\left(\ln\tan\frac{\delta}{2} + \sec\delta\right)\tan\delta + 2fc_2\theta\tan\delta \\ w(\delta) &= -c_1\cos\delta - 2f\left(\Delta T\alpha_{11} - \Delta T\alpha_{22} + c_2\right)\left(\cos\delta\ln\tan\delta + \sec\delta\right) + f\alpha_{11}\Delta T\sec\delta \end{aligned} \tag{16}$$

To eliminate the singularity in the expressions of u and w at $\delta = 0$, we assume that $c_2 = -\left(\Delta T\alpha_{11} - \Delta T\alpha_{22}\right)$, and Eq.(16) is further simplified as,

$$\begin{aligned} u(\delta) &= \alpha_{11}\Delta T f\sin\delta\sec^2(\delta) + c_1\sin\delta \\ v(\delta,\theta) &= 2f\Delta T\alpha_{12}\left(\ln\tan\frac{\delta}{2} + \sec\delta\right)\tan\delta - 2f\Delta T\left(\alpha_{11} - \alpha_{22}\right)\tan(\delta)\theta \\ w(\delta) &= -c_1\cos\delta + f\alpha_{11}\Delta T\sec(\delta) \end{aligned} \tag{17}$$

Since there exits no singularity in Eq.(17), c_1 can be derived directly from the boundary conditions $w(0) = 0$, which gives $c_1 = f\alpha_{11}\Delta T$. Then, the displacement solution for each segment antenna in Eq. (17) is further expressed as,

$$\begin{aligned} u(\delta) &= \alpha_{11}\Delta T f\sin\delta\left(\sec^2\delta + 1\right) \\ v(\delta,\theta) &= -2f\Delta T\left(\alpha_{11} - \alpha_{22}\right)\left(\tan\delta\right)\theta \\ w(\delta) &= \alpha_{11}\Delta T f\cos\delta\left(\sec^2\delta - 1\right) \end{aligned} \tag{18}$$

Applying Eq. (17), the magnitudes of the displacement fields $\sqrt{u^2(\delta) + v^2(\delta) + w^2(\delta)}$ of one piece segment of antenna reflector (the diameter is 2 m, the focal length is $f = 0.5$ m, and $\Delta T = 200$ °C) are predicted and compared with the FEA results, as shown in Fig. 5. Note, the results for the case of composite ply-angle $\vartheta = 45°$ are not presented in Fig. 5, as they are identical with that of a continuous surface reflector presented in Fig. 2. In Fig. 5, the prediction results given by Eq. (17) match well with the FEA results, which also approve that the assumption of $c_2 = -\left(\Delta T\alpha_{11} - \Delta T\alpha_{22}\right)$ is appropriate. For the cases of composite ply angles $\vartheta = 30°$ and $\vartheta = 60°$, the magnitudes of the thermal displacement fields for the segmented antenna reflector at $\theta = 0°$ and $\vartheta = \pm 30°$ as presented in Fig. 5 significantly decreased compared with the numerical results shown in Fig. 2.

We further segment the antenna reflector along the meridional direction resulting 12 segmented pieces, each of which is mounted at their own individual central, as illustrated in Fig. 6. The membrane state of the antenna reflector remains, thus Eq.(17) together with Eq.(13) can be used to compute the displacement fields of each segment of the

antenna reflector in a Cartesian coordinate system, by introducing an additional translation components as,

$$\begin{aligned} U(x,y) &= U(x,y) - U(x_i,y_i) \\ V(x,y) &= V(x,y) - V(x_i,y_i) \\ W(x,y) &= W(x,y) - W(x_i,y_i) \end{aligned} \tag{19}$$

where (x_i, y_i) denotes the central coordinates of reflector segments. Eq. (19) illustrates a physical translation procedure that the deformation of each piece of segmented antenna reflector is initially computed with respect to the mounted paraboloid vertex, and then the computation is translated with respect to a position that the displacements of its own central point are zero. The magnitudes of the displacement fields for the antenna reflector shown in Fig. 6 are predicted via both the theoretical model and the FEA simulation, and the results are presented and compared in Fig. 7. Due to a further segmenting along the meridional direction, the displacement fields are piece-wise functions and the deformation results presented in Fig. 7 are apparently further reduced compared with the results shown in Fig. 5. The preliminary analysis results presented in Fig. 5 and Fig. 7 clearly demonstrate that the segmenting design method provides an effective means to lower the thermal deformation of the antenna reflector. It is also interesting to note that the displacement in Fig. 7-(b) for the case of ply-angle $\vartheta = 45^\circ$ is a one order of magnitude less than that of both Fig. 7-(a) and 7-(c), which present the results given by the ply-angle of $\vartheta = 30^\circ$ and $\vartheta = 60^\circ$, respectively. This phenomenon can also be observed from the RMS$[\Delta_i]$ trend varying with respect to the ply angles ϑ as shown in the following Fig. 8, and it also matches with the conclusion drawn from the analysis based on our analytical model (as discussed in the later paragraph).

From the mechanical response point of view, there are two major reasons that the segmented antenna reflector can successfully suppress the thermal deformations compared with a continuous surface antenna, as demonstrated in the above simulation results. Firstly, the radial edges of a circular section in a continuous surface antenna are constrained $v(\delta) = 0$, which can be considered as the virtual boundary condition of each circular section. In contrast, the radial edges of a circular section (one-piece segment) of the segmented antenna are completely free. The release of the constraints along the radial edges for each segment results in an overall mitigation of thermal deformations for the segmented antenna. This mechanism is much more obvious when non-uniform temperature fields are applied, as shown in Figs. 20-21 in section V. Based on our theoretical model derived from the thin shell theory, it indicates that the terms related to $(\alpha_{11} - \alpha_{22})$ in Eq. (17) result in the main thermal displacement difference between a continuous antenna and a segmented antenna. Secondly, for the segmented antenna, each piece of segment has its own mounting point, at which the deformation is constrained to be zero. Around the local region of these mounted points, the thermal deformations are suppressed to a great extent. As a result, the thermal deformations of the entire region of the segmented antenna are decreased, significantly. Note, for the computation of the deformation fields of each segment of the antenna reflector

requires an additional physical translation procedure given by the above Eq. (19), with which the deformation of each piece of segmented antenna reflector is initially computed with respect to the mounted paraboloid vertex, and then translated with respect to its own mounting point. Eq. (19) for the translation procedure is the mathematical reason that leads the thermal deformation for each piece of segmented antenna reduced, significantly.

Applying the theoretical model, the RMS$[\Delta_i]$ values of the segmented antenna reflector in Fig. 6 with different ply angles are predicted using the analytical model, and the obtained results are presented in Fig. 8. The variation of the RMS$[\Delta_i]$ values with respect to the ply angles (ϑ) presented in Fig. 8 for the segment antenna reflector has a similar trend with that presented in Fig. 5 for the continuous surface reflector. However, the RMS$[\Delta_i]$ values become much lower than for all the cases of ply angles after the antenna reflector is segmented.

The RMS$[\Delta_i]$ for the segmented antenna reflector meets the lowest value 44 μm when $\vartheta = 45\ ^\circ$, which offers 70.1% decrease compared with the corresponding value of a continuous surface antenna reflector. Both Fig. 3 and Fig. 8 show that the ply angle $\vartheta = 45^\circ$ for the composite shell lay-up $[\pm\vartheta/\mp\vartheta/core/\pm\vartheta/\mp\vartheta]$ gives the lowest surface error of RMS$[\Delta_i]$. The surface accuracy of the segmented antenna reflector is further analyzed to investigate the effects given by the number of segments. Note, for a segmented antenna reflector, each segment is mounted on its own central. An analysis for the surface accuracy with respect to the number of segment is carried out using a parametric study. The results, as shown in Fig. 9, clearly show that the surface accuracy of a segmented antenna reflector can be substantially elevated through increasing the number of segments, and also illustrates that RMS$[\Delta_i]$ is more sensitive to the segment number along the meridional direction. With a segment number of 8×6, the RMS$[\Delta_i]$ of the antenna reflector achieves as low as 9.83 μm.

In this study, the development of theoretical model based on Sanders improved first-approximation thin shell theory is not only used to verify our finite element model (with each other), but also provide us an alternative and efficient tool to perform the analysis during the preliminary design process for segmented antennas, for example, the parametric studies for the RMS surface error that have been presented in the Figs. 8 and 9. In addition, this theoretical model enables us to obtain a deep understanding for the physical mechanism of this problem, as well as the relevant parameters in relation with the thermal deformations of either a continuous or a segmented antenna surface. For example, for a membrane state antenna reflector under a uniformly distributed temperature loading, the magnitudes of the thermal deformation are approximately linear with the temperature variation ΔT or its focal length f. There are quite many terms of $(\alpha_{11} - \alpha_{22})$ that are involved in the analytical solutions for the antenna-surface thermal deformations given by Eqs. (11) and (18). This indicates that the (composite) materials with two equal coefficients of thermal expansions, namely $\alpha_{11} = \alpha_{22}$, will lead to relatively low thermal deformations. This conclusion is also verified by the cases of composite ply-angle $\vartheta = 45^\circ$ in Figs. 2 and 5.

IV. Thermally Stable Grid Structure (TSGS)

In all of the above analysis, we assumed that the central points of the antenna segments are mounted as fixed points. However, in practice, the antenna segments are usually mounted on a supporting structure. Therefore, it is expected that the supporting structure has no thermal deformation, or at least there is no thermal displacement at the mounting point. To this end, a novel thermally stable grid structure is proposed and designed, which is introduced in this section.

In principle, the CFRPs can be designed to possess zero equivalent thermal expansion coefficient, however, in the practical manufacturing process, it is very difficult to control the volume ratio of matrix and carbon fibers, the fiber angles and ply thicknesses precisely. Therefore, in practice, CFRP materials with zero thermal expansion coefficients are hardly to be achieved. This is also a major reason that many research works make effort in suppressing thermal deformations for space antennas [3, 22, 24]. Instead of directly applying unrealistic materials with perfect zero thermal expansion coefficient, our strategy is to design a novel thermal-insensitive structural form, namely Thermally Stable Grid Structure (TSGS). With the design of TSGS, the thermal deformation of the mounting center of each antenna segment will maintain a minimum level under various thermal loading conditions.

The basic design principle of this TSGS is illustrated with a typical cell structure, which is a symmetric yet irregular hexagon composite box, as shown in Fig.10. A cell structure of TSGS consists of a hexagon CFRP frame and an internal Aluminum web. The working mechanism of this hexagon cell structure is that its thermal deformations (either expansion or shrink) along one direction (defined as x) can be largely compensated by the thermal deformation of the Aluminum web and internal structural coupling. For instance, when the temperature is increased, the whole CFRP frame will expand along both directions if the internal Aluminum web is not applied. However, due to the existence of this Aluminum web and its thermal expansion, both of the top two side-walls and the bottom two side-walls will be expanded outward and the inner angles between them are decreased, which will then pull back the vertical side-walls to the original positions for a certain extent. As a consequence, the thermal expansion of the whole hexagon frame along the x direction is largely suppressed. Similarly, the thermal shrink of the hexagon cell along the x direction is prevented by the Aluminum web when the temperature is decreased.

To further validate the working mechanism of this proposed TSGS, the thermal deformations of a cell structure under the temperature variation of 200 °C and −200 °C are predicted by ABAQUS, and are presented in Fig. 11. The lay-up of the composite frame is $[0_{0.5\text{mm}}/90_{0.5\text{mm}}/90_{0.5\text{mm}}/0_{0.5\text{mm}}]$. The cell of TSGS is modeled by shell element S4R, and a symmetric boundary condition is applied. The hexagon cell structure is allowed to deform freely except that the rotation of its corners are restrained, as illustrated in the first plot of Fig. 11. Under the temperature variation of ±200 °C, although the cell structure has obvious shrink or expansion along the y direction, its thermal deformation along the x direction is almost negligible. FEA results show that the thermal deformation of the internal Aluminum web is much larger than that of the CFRP frame walls. When the cell structure is heated, the expansion of the internal Aluminum web will push out both of the top and the bottom side-walls and then give rise to compressive forces to the

frame, which then shrink back the expanded CFRP frame along the x direction. Consequently, the elastic shrinks of the vertical side-walls caused by the compressive force of the Aluminum wall compensate the thermal expansion of the entire CFRP frame along the x direction. Conversely, if the cell structure is cooling down, the internal Aluminum web will give rise to tension forces on the CFRP frame, which will prevent the elastic shrinks of the CFRP frame resulting in negligible overall deformation along the x direction. Furthermore, a parametric study has also been carried out with FEA to obtain the optimal dimensions for this proposed thermal stable mechanism as presented in Fig. 10. In this parametric study, the wall thickness of 2 mm and the frame height of 30 mm along the z direction, and the frame length of 50 mm along the x direction are fixed, whilst the Aluminium web length along the y direction is adjustable. After a series of simulations, the dimension of 53 mm along the y direction for the Aluminium web is found to be an optimal value for minimizing the thermal deformation along the x direction.

Based on this thermal stable hexagon cell structure, a complete form of Thermally Stable Grid Structure (TSGS) is designed to support each segment of the segmented antenna reflector, as presented in Fig. 12. A segmented antenna with 12 pieces is supported by 6 TSGS structures, each of which can support two segmented parts. The diameter of the antenna is 2 m, and the focal length f = 0.5 m. The TSGS are mounted on a CFRP ring, which is mounted onto a spacecraft or a satellite. A TSGS has a short arm and a long arm for supporting the inner side and the outer side antenna segmented parts, respectively. The short and long arms of the TSGS are constituted by 3 and 12 hexagon cells, respectively. For each hexagon cell, its boundary condition is identical with that illustrated in Fig. 11. The thermal deformations of a typical TSGS are predicted by FEA. The geometry and the composite layups for this finite element model are shown in the first plot of Fig. 13, and the thin-walled structures in this TSGS are modeled using the shell elements S4R. The thermal displacement-contours of this TSGS under a temperature variation 200 °C and -200 °C are presented in Fig. 13, respectively. The FEA results clearly demonstrated that the thermal deformations at the supporting points of both the short arm and the long arm are very small, only about 23 μm and 10 μm, respectively.

To further validate the static stiffness of this proposed TSGS, a modal analysis is carried out on a one-sixth part of the antenna supported by a single TSGS, as shown in Fig. 14. The TSGS is mounted at the buttons. The lay-up of the antenna reflector is $[45/-45/-45/45/\text{core}/45/-45/-45/45]$. The thickness of the CFRP skin is 0.4 mm and the thickness of honeycomb core is 19.2 mm. The mass of the complete antenna reflector is 8.21 Kg and the mass of a single TSGS is 0.533 Kg. The antenna reflector is also modeled by shell elements S4R. The fundamental frequency of the antenna is 2.56 Hz. The modal analysis results given by FEA demonstrated that the TSGS has enough stiffness for supporting the reflector.

In this section, the thermal deformation of TSGS under a uniform temperature thermal loading is analyzed, and it approves the proposed design principle of TSGS, which has excellent thermal stability at the mounting points of antenna segments. In the next section, the surface accuracy of the complete antenna which composes of the antenna reflector and the supporting TSGS is analyzed and discussed.

V. Antenna Surface Accuracy Analysis

The thermal deformation of the segmented antenna is predicted using FEA. Both of the antenna reflector and the TSGS are modeled by shell elements S4R. Note, in this section, an antenna reflector with 2 m diameter and $f = 0.5$ m focal length is studied. Under a uniform temperature thermal loading of 200 °C, the predicted contours of the thermal deformations of a complete segmented antenna supporting by TSGS and a segmented antenna with each segment that is artificially mounted at their own central are presented and compared in Fig. 15. Note, the gaps between each reflector segments are 5 mm. FEA shows that the displacement magnitudes at the supporting points of the segmented antenna are very small, only about $10 \sim 20\ \mu m$. The calculated RMS surface errors RMS$[\Delta_i]$ of the complete segmented antenna and the artificially mounted reflector are 69.6 μm and 59.6 μm, respectively. It approves that applying the designed TSGS to support the segmented antenna results in very limited influence on the thermal deformations, and thus the surface accuracy of the segmented antenna.

The antenna is manufactured at room temperature, i.e., 20 °C. When it is launched into the orbit, the temperature variation of the antenna is usually not uniform, due to the non-uniform projection of sun heating flux or earth infrared radiation. To quantitatively investigate the influence of non-uniform temperature variation, we predict the thermal deformation of the segmented antenna with different non-uniform temperature variations. The surface errors RMS$[\Delta_i]$ of the antenna reflector under six different settings of the non-uniform temperature variation are studied, as illustrated in Fig. 16. The region marked by red has a temperature variation of 200 °C. The thermal deformations of both the continuous surface antenna and the segmented antenna are predicted using FEA, and the corresponding values of RMS$[\Delta_i]$ are computed and presented in Fig. 16. The variation of the RMS surface error is nonlinear for the continuous surface antenna. A local temperature variation may lead to the increased RMS surface error, since the local thermal stress may induce severe local distortions in a continuous reflector due to the structural continuity. In other words, for a continuous surface antenna reflector, the temperature variation should be well suppressed in the whole region of the antenna reflector for achieving the small RMS surface error. On the contrary, the surface error of the segmented antenna almost linearly varies with the percentage of the high temperature region, because the thermal deformations of reflector segments are uncoupled. The thermal deformation that occurs on one reflector segment has no influence on the other segments. As a consequence, the segmented antenna reflector has another advantage, namely in a complex thermal environment, the influence of a local temperature variation is limited, and will not cause severe degradation of overall surface accuracy of reflector.

To simulate the RMS surface error of the segmented antenna in real space environment, a segmented antenna and a continuous surface antenna are installed on a simple cube satellite, respectively, and launched into the geosynchronous orbit. The thermal analysis of the satellites are conducted by the commercial software NX[37], and Fig. 17 presents the thermal analysis model of the satellite. The orbit setup for the satellite is illustrated in Fig. 18. The temperature field of the antenna is calculated at an interval of every 1.5 hour. In this thermal analysis model, the detailed setups for thermal

parameters are presented in Table. 2.

Table 2 (Surface) Thermal parameters used in thermal analysis model

Antenna reflector	Surface thermal absorptivity 0.4 Surface infrared emittance 0.87
Satellite main structure	Surface thermal absorptivity 0.4 Surface infrared emittance 0.68
Solar panel	Front surface thermal absorptivity 0.7 Front surface infrared emittance 0.92 Back surface thermal absorptivity 0.88 Back surface infrared emittance 0.92
CFRP structure material	Specific heat 0.712 kJ/kg·K Heat conductive coefficient 10 W/m· k

The temperature fields of the satellites with both of segmented and continuous surface antenna under a same space thermal environment are predicted and analyzed. The variances of the temperature field and the average temperatures of the segmented and continuous surface antenna reflectors during the days of winter solstice and vernal equinox are calculated and presented in Fig. 19. The average temperature and the temperature variances of the segmented antenna reflector are similar with those of the continuous surface antenna reflector in both winter solstice and vernal equinox. At the time 18 : 00, the temperature of the antenna is nearly uniform, the average temperatures are the lowest, which are about -115 °C. At the time 4 : 30 and 21 : 00, the variances of temperature fields reach local maximum points, which indicate the temperature fields at the time of 4 : 30 and 21 : 00 are much more non-uniform than the other time.

The temperature fields at 4 : 30, 18 : 00 and 21 : 00 in winter solstice are also predicted and presented in Fig. 20. However, the temperature field of the segmented antenna is much different from that of the continuous surface antenna, this is because that the thermal conduction between each antenna segment is impeded due to the segmenting gaps. Applying the finite element analysis (FEA), the thermal deformations of both the segmented and continuous surface antennas at the time 4 : 30, 18 : 00 and 21 : 00 are predicted by mapping the temperature fields to the finite element analysis models, respectively. The predicted displacement contours of segmented and continuous surface antennas in winter solstice are presented in Fig. 21. Compared the contour plots in left-hand side (the segmented antenna) with that in right-hand side (the continuous surface antenna) in Fig. 21, the majority regions of the segmented antenna-surface show much lower magnitudes of thermal deformation (indicated by a large amount of blue areas) than that of the continuous antenna-surface. In other words, Fig. 21 clearly demonstrated that applying a segmented antenna can largely suppress the thermal deformation in a practical space environment compared with a continuous surface antenna. FEA results also indicate that, for a segmented antenna, the thermal displacements at the mounting points are very small, thus the influence of TSGS is very limited and negligible. The displacement contours during the period of vernal equinox are similar with those in winter solstice, and are not presented herein. The RMS surface errors of the two antenna reflectors are calculated and presented in Table. 3. In the geosynchronous orbit, although the temperature

fields of the two antennas are similar, the surface accuracy of the segmented antenna is much better than that of the continuous surface antenna. The maximum RMS surface error of the segmented antenna is only about 37.7μm, whilst the maximum RMS surface error of the continuous surface antenna is about 94μm.

Table 3 RMS surface errors of antenna reflectors at different times, predicted by finite element method. The temperature fields of the antenna reflectors in the geosynchronous orbit are applied.

Day	winter solstice			vernal equinox		
Time	4:30	18:00	21:00	4:30	18:00	21:00
RMS$[\Delta_i]$ (μm) for a segmented antenna reflector	9.5	29.8	18.3	13.7	37.7	18.2
RMS$[\Delta_i]$ (μm) for a continuous surface antenna reflector	23.1	92.2	52.7	28.2	94.0	47.0

VI. Conclusion

In this study, a novel design method is proposed to elevate the surface accuracy of paraboloid solid surface antenna reflector through dividing the antenna reflector into a certain number of segments. To approve the design principle and working mechanism of this proposed segmenting method, a simplified analytical model for predicting the thermal deformation of both the segmented antenna reflector and the continuous surface reflector is developed. Based on this analytical model, the RMS surface errors of a segmented antenna reflector and a continuous antenna reflector with the diameter of 2 m are calculated and compared. The predicted results demonstrated that the RMS surface error of a segmented antenna reflector with 2×6 pieces offers at least 70% improvement on surface accuracy compared with that of a continuous surface antenna reflector. The RMS surface error can be further decreased if the antenna reflector is divided into more pieces of segments. Furthermore, a novel design of Thermally Stable Grid Structure (TSGS) with one short arm and a long arm is proposed to support each piece of the segmented antenna reflector. The most distinct advantage of this novel TSGS is that it can largely suppress the thermal deformations at the joints (supporting points), by means of using an internal Aluminium web to compensate the thermal deformations along the mounting-point direction. The design principle and working mechanism of this TSGS is approved numerically using finite element analysis. The numerical results show that the segmented antenna reflector supported by the TSGS outperforms the continuous antenna reflector for all the cases of working scenarios. The FEA results further show that, in the geosynchronous orbit, the maximum RMS surface error of a continuous antenna reflector with the diameter of 2 m is 95 μm, whilst the maximum RMS surface error of the segmented antenna reflector with 12 segments is only about 20 μm. In summary, the proposed segmenting method along with the TSGS technique can largely suppress the RMS surface error of antenna reflector in a passive manner, which offers a number of advantages in practical applications over an active control based system. The novel design of both the segmented antenna reflector and the TSGS have a great potential to be extended for applying in

other forms of antennas, e.g. deployable antennas.

A. Appendix

A. The derivation of a new formula for RMS$[\Delta_i]$

To derive the RMS$[\Delta_i]$, a new paraboloid surface is fitted according to the thermal deformation of the antenna reflector. A new Cartesian coordinate is established for this new fitted paraboloid surface, as illustrated in Fig. 22. This new coordinate system has a translation of (u_a, v_a, w_a) from the origin of the old Cartesian coordinate system along each axis, respectively, and also rotates an angle of φ_x, φ_y and φ_z to each original x, y and z axis, respectively. The relationship between the new and the old coordinate system is given by,

$$\begin{aligned} x_1 &= x - u_a - z\varphi_y \\ y_1 &= y - v_a + z\varphi_x \\ z_1 &= z - w_a + x\varphi_y - y\varphi_x \end{aligned} \tag{20}$$

In the deviation of Eq. (20), the rotation with respect to z axis is omitted, because this paraboloid surface is axisymmetric with respect to z axis. Since the rotation angles φ_x and φ_y are very small, the small-angle approximation $\cos\varphi_x = \cos\varphi_y \approx 1$, $\sin\varphi_x \approx \varphi_x$ and $\sin\varphi_y \approx \varphi_y$ is applied to simplify our derivation. In this new coordinate system, assuming the focal length of the fitted paraboloid surface has a change of Δf, the fitted paraboloid surface is defined by the following expression,

$$z_1 = \frac{1}{4(f+\Delta f)}\left(x_1^2 + y_1^2\right) \tag{21}$$

Substituting Eq. (20) into Eq. (21), the fitted paraboloid surface expressed in terms of the old Cartesian coordinate system is derived as,

$$x^2 + y^2 + 2zy\phi_x - 2zx\phi_y - 2x(u_a + 2f\phi_y) - 2y(v_a - 2f\phi_x) - 4z(f+\Delta f) + 4fw_a = 0 \tag{22}$$

Note, in Eq. (22), the high order terms are neglected. The direction cosine of the normal vector for the original paraboloid surface at the node (x_i, y_i, z_i) are,

$$\begin{aligned} \cos\alpha_1 &= -\frac{x_i}{2\sqrt{f(f+z_i)}} \\ \cos\alpha_2 &= -\frac{y_i}{2\sqrt{f(f+z_i)}} \\ \cos\alpha_3 &= \frac{f}{\sqrt{f(f+z_i)}} \end{aligned} \tag{23}$$

If the translation vector of the node (x_i, y_i, z_i) is (u_i, v_i, w_i), the distance between the node (x_i, y_i, z_i) after deforming and the fitted paraboloid surface is Δ_i,

$$\begin{aligned} x - (x_i + u_i) &= \pm\Delta_i \cos\alpha_1 \\ y - (y_i + v_i) &= \pm\Delta_i \cos\alpha_2 \\ z - (z_i + w_i) &= \pm\Delta_i \cos\alpha_3 \end{aligned} \tag{24}$$

where x, y, z are the coordinates of a node on the fitted paraboloid surface. Substituting Eq. (24) into Eq. (22), the expression for Δ_i is derived,

$$\begin{aligned} \Delta_i = \pm\frac{1}{2\sqrt{f(f+z_i)}} \big[& x_i\,(u_i - u_a) + 2f\,(w_i - w_a) - 2z_i h + \\ & y_i\,(2f + z_i)\,\phi_x - x_i\,(2f + z_i)\,\phi_y \big] \end{aligned} \tag{25}$$

Applying the least squares method, the unknown parameters of the fitted paraboloid surface can be solved by a group of linear algebraic equations as,

$$\frac{\partial G}{\partial u_a} = \frac{\partial G}{\partial v_a} = \frac{\partial G}{\partial w_a} = \frac{\partial G}{\partial \phi_x} = \frac{\partial G}{\partial \phi_y} = \frac{\partial G}{\partial h} = 0, \quad G = \sum_1^N \Delta_i^2 \tag{26}$$

Substituting Eq. (26) into Eq. (25), a new formula for $\mathrm{RMS}[\Delta_i]$ is finally derived and given by,

$$\mathrm{RMS}[\Delta_i] = \sqrt{\frac{G}{N}} \tag{27}$$

B. The derivation for equivalent thermal expansion coefficients of a composite shell

The equivalent thermal expansion coefficients α_{11}, α_{22} and α_{12} are obtained by solving the following linear equations,

$$\begin{bmatrix} A_{11} & A_{12} & A_{16} \\ A_{12} & A_{22} & A_{26} \\ A_{16} & A_{26} & A_{66} \end{bmatrix} \begin{bmatrix} \alpha_{11} \\ \alpha_{22} \\ \alpha_{12} \end{bmatrix} = \sum_{i=1}^{n} t_i \begin{bmatrix} \overline{Q}_{11}^i & \overline{Q}_{12}^i & \overline{Q}_{16}^i \\ \overline{Q}_{21}^i & \overline{Q}_{22}^i & \overline{Q}_{26}^i \\ \overline{Q}_{16}^i & \overline{Q}_{26}^i & \overline{Q}_{66}^i \end{bmatrix} \begin{bmatrix} \overline{\alpha}_{11}^i \\ \overline{\alpha}_{22}^i \\ \overline{\alpha}_{12}^i \end{bmatrix} \tag{28}$$

where t_i denotes the thickness of the i-th ply. $\overline{\alpha}^i_{ij}(i,j=1,2)$ are the thermal expansion coefficients of the i-th ply. For composite laminates, $\overline{\alpha}^i_{ij}(i,j=1,2)$ are determined from the following transformation equation,

$$\begin{bmatrix} \overline{\alpha}^i_{11} \\ \overline{\alpha}^i_{22} \\ \overline{\alpha}^i_{12} \end{bmatrix} = [T^i]^T \begin{bmatrix} \alpha^o_1 \\ \alpha^o_2 \\ \alpha^o_{12} \end{bmatrix}^{(i)} \tag{29}$$

where α^o_1 and α^o_2 denote the thermal expansion coefficients of an orthotropic lamina in principal material coordinates, and the values that are used in this study have been given in Table 1. Matrix $[T]$ is the standard transformation matrix for composite laminates, e.g. defined by Eq. (2.76) (page 75) in [12].

Acknowledgments

The authors sincerely acknowledges the financial support from Ningbo University, Zhejiang Province, China.

References

[1] Archer, J. S., "High-Performance Parabolic Antenna Reflectors," *Journal of Spacecraft and Rockets*, Vol. 17, No. 1, 1980, pp. 20–26. https://doi.org/10.2514/3.57702.

[2] Sharp, G. R., Gilger, L. D., and Ard, K. E., "Extreme Precision Antenna Reflector Study Results," *NASA Reference Publication*, Vol. NASA-CP-2368-PT-1, April 01, 1985.

[3] Ozaki, T., Naito, K., Mikami, I., Yamauchi, H., and Tsuneta, S., "High precision composite pipes for SOLAR-B optical structures," *Acta Astronautica*, Vol. 48, No. 5, 2001, pp. 321 – 329. https://doi.org/10.1016/S0094-5765(01)00027-3.

[4] Soykasap, O., and Tan, L. T., "High-precision offset stiffened springback composite reflectors," *AIAA journal*, Vol. 49, No. 10, 2011, pp. 2144–2151. https://doi.org/10.2514/1.J050846.

[5] Klimm, W., and Kwok, K., "Surface Accuracy of Viscoelastic Composite Thin-Shell Deployable Reflector Antennas," *AIAA Scitech 2020 Forum*, 2020. https://doi.org/10.2514/6.2020-0932.

[6] Liu, Z.-Q., Qiu, H., Li, X., and Yang, S.-L., "Review of large spacecraft deployable membrane antenna structures," *Chinese Journal of Mechanical Engineering*, Vol. 30, No. 6, 2017, pp. 1447–1459. https://doi.org/10.1007/s10033-017-0198-x.

[7] Rogers, C., Stutzman, W., Campbell, T., and Hedgepeth, J., "Technology assessment and development of large deployable antennas," *Journal of Aerospace Engineering*, Vol. 6, No. 1, 1993, pp. 34–54. https://doi.org/10.1061/(ASCE)0893-1321(1993)6:1(34).

[8] Huang, H., Guan, F.-L., Pan, L.-L., and Xu, Y., "Design and deploying study of a new petal-type deployable solid surface antenna," *Acta Astronautica*, Vol. 148, 2018, pp. 99–110. https://doi.org/10.1016/j.actaastro.2018.04.042.

[9] Freeland, R., and Veal, G., "Significance of the inflatable antenna experiment technology," *39th AIAA/ASME/ASCE/AHS/ASC Structures, Structural Dynamics, and Materials Conference and Exhibit*, 1998, p. 2104. https://doi.org/10.2514/6.1998-2104.

[10] Cassapakis, C., and Thomas, M., "Inflatable structures technology development overview," *Space programs and technologies conference*, 1995, p. 3738. https://doi.org/10.2514/6.1995-3738.

[11] Crone, G., "Large deployable reflector antenna for advanced mobile communications," *ESA/Ind Br Meet*, Vol. 9, 2000, pp. 4–20. https://doi.org/10.1007/s12567-013-0044-7.

[12] Jones, R. M., *Mechanics of composite materials*, CRC press, 1998.

[13] Love, A., "Some highlights in reflector antenna development," *Radio Science*, Vol. 11, No. 8-9, 1976, pp. 671–684. https://doi.org/10.1029/RS011i008p00671.

[14] Campbell, T., Butler, D., Belvin, K., and Allen, B., "Development of the 15-meter hoop-column antenna system," *lsas*, 1985, pp. 167–212. https://doi.org/10.1016/0094-5765(88)90130-0.

[15] Miura, K., and Miyazaki, Y., "Concept of the tension truss antenna," *AIAA Journal*, Vol. 28, No. 6, 1990, pp. 1098–1104. https://doi.org/10.2514/3.25172.

[16] Thomson, M., "AstroMesh™ deployable reflectors for ku and ka band commercial satellites," *20th AIAA international communication satellite systems conference and exhibit*, 2002, p. 2032. https://doi.org/10.2514/6.2002-2032.

[17] Datashvili, L., Endler, S., Wei, B., Baier, H., Langer, H., Friemel, M., Tsignadze, N., and Santiago-Prowald, J., "Study of mechanical architectures of large deployable space antenna apertures: from design to tests," *CEAS Space Journal*, Vol. 5, No. 3-4, 2013, pp. 169–184. https://doi.org/10.1007/s12567-013-0050-9.

[18] Im, E., Thomson, M., Fang, H., Pearson, J., Moore, J., and Lin, J., "Prospects of large deployable reflector antennas for a new generation of geostationary Doppler weather radar satellites," *AIAA SPACE 2007 Conference & Exposition*, 2007, p. 9917. https://doi.org/10.2514/6.2007-9917.

[19] Suenaga, M., and Prevaux, R. J., "MBSAT A direct broadcast satellite for mobile users in Japan and Korea," *Acta Astronautica*, Vol. 57, No. 2-8, 2005, pp. 215–223. https://doi.org/10.1016/J.ACTAASTRO.2005.03.026.

[20] Guest, S., and Pellegrino, S., "A new concept for solid surface deployable antennas," *Acta Astronautica*, Vol. 38, No. 2, 1996, pp. 103 – 113. https://doi.org/10.1016/0094-5765(96)00009-4.

[21] Imbriale, W. A., Gao, S. S., and Boccia, L., *Space antenna handbook*, John Wiley & Sons, 2012. https://doi.org/10.1002/9781119945147.

[22] Cofield, R. E., and Kasl, E. P., "Thermal stability of a 4 meter primary reflector for the scanning microwave limb sounder," *Earth Observing Systems XVI*, Vol. 8153, International Society for Optics and Photonics, 2011, p. 81530Y. https://doi.org/10.1117/12.893890.

[23] Abusafieh, A. A., Federico, D. R., Connell, S. J., Cohen, E. J., and Willis, P. B., "Dimensional stability of CFRP composites for space-based reflectors," *Optomechanical Design and Engineering 2001*, Vol. 4444, International Society for Optics and Photonics, 2001, pp. 9–16. https://doi.org/10.1117/12.447300.

[24] Tanaka, S., Ikeda, T., and Senba, A., "Sensitivity analysis of thermal deformation of CFRP laminate reflector due to fiber orientation error," *Journal of Mechanical Science and Technology*, Vol. 30, No. 10, 2016, pp. 4423–4426. https://doi.org/10.1007/s12206-016-0905-z.

[25] Bradford, S., Agnes, G., Ohara, C., Shi, F., Peterson, L., Hoffman, S., and Wilkie, K., "Piezocomposite actuator arrays for correcting and controlling wavefront error in reflectors," *53rd AIAA/ASME/ASCE/AHS/ASC Structures, Structural Dynamics and Materials Conference, 20th AIAA/ASME/AHS Adaptive Structures Conference 14th AIAA*, 2012, p. 1743. https://doi.org/10.2514/6.2012-1743.

[26] Pawlik, E., Lin, R., and Fichter, W., "NASA's Precision Segmented Reflectors (PSR) Project," *Active telescope systems*, Vol. 1114, International Society for Optics and Photonics, 1989, pp. 374–386. https://doi.org/10.1117/12.960842.

[27] Lehman, D. H., Pawlik, E. V., Meinel, A. B., and Fichter, W., "Precision segmented reflectors for space applications," *Adaptive optics and optical structures*, Vol. 1271, International Society for Optics and Photonics, 1990, pp. 191–203. https://doi.org/10.1117/12.20407.

[28] Bush, H. G., Herstrom, C. L., Heard Jr, W. L., Collins, T. J., Fichter, W., Wallsom, R. E., and Phelps, J. E., "Design and fabrication of an erectable truss for precision segmented reflector application," *Journal of Spacecraft and Rockets*, Vol. 28, No. 2, 1991, pp. 251–257. https://doi.org/10.2514/6.1990-999.

[29] Collins, T. J., and Fichter, W., "Support trusses for large precision segmented reflectors: Preliminary design and analysis," *Active telescope systems*, Vol. 1114, International Society for Optics and Photonics, 1989, pp. 453–469. https://doi.org/10.1117/12.960848.

[30] Miller, R. K., *Concepts and Analysis for Precision Segmented Reflector and Feed Support Structures*, Vol. 182064, National Aeronautics and Space Administration, Langley Research Center, 1990.

[31] Yao, Z., Wu, T., Zhou, Y., and Fang, H., "Surface Accuracy Study for a Segmented Reflector," *AIAA Scitech 2019 Forum*, 2019. https://doi.org/10.2514/6.2019-0753.

[32] Sanders, J. L., *An improved first-approximation theory for thin shells*, Vol. 24, US Government Printing Office, 1960.

[33] Farshad, M., *Design and analysis of shell structures*, Vol. 16, Springer Science & Business Media, 1992. https://doi.org/10.1007/978-94-017-1227-9.

[34] Radwanska, M., Stankiewicz, A., Wosatko, A., and Pamin, J., *Plate and shell structures*, Wiley Online Library, 2016. https://doi.org/10.1002/9781118934531.

[35] Love, A. E. H., *A treatise on the mathematical theory of elasticity*, Cambridge university press, 2013.

[36] Inagaki, A., Sakamoto, H., Tanaka, H., Ishimura, K., and Okuma, M., "Experimental Study of Reflector Shape Control under Various Thermal Conditions," *2nd AIAA Spacecraft Structures Conference*, 2015. https://doi.org/10.2514/6.2015-1399.

[37] *Siemens NX12.0 User's Manual*, Siemens Industry Software, Inc., 2017.

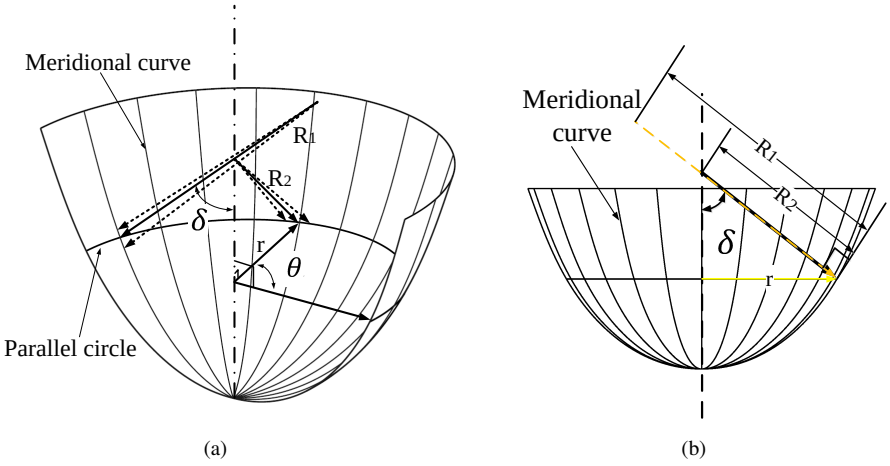

Fig. 1 The co-ordinate system of a paraboloid shell of revolution

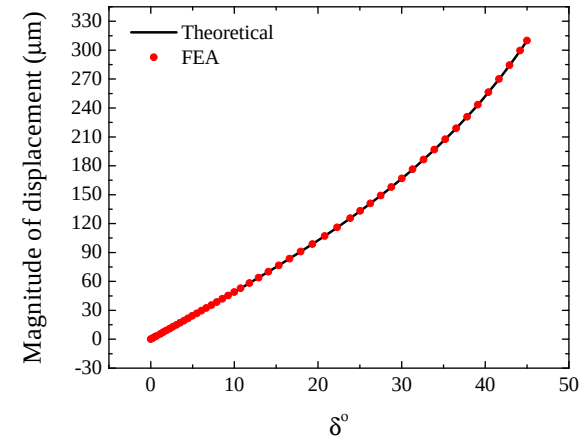

(a) $\vartheta = 45°$

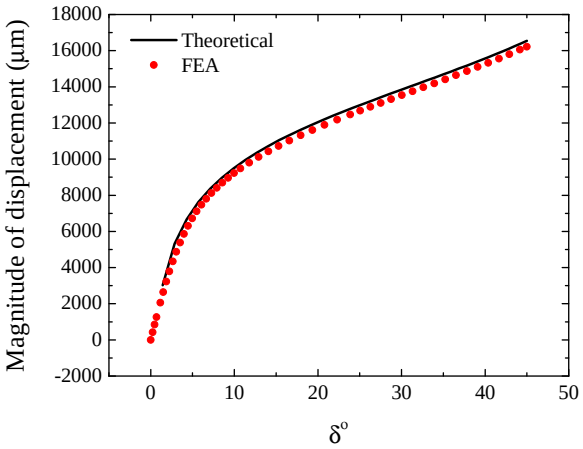

(b) $\vartheta = 60°$

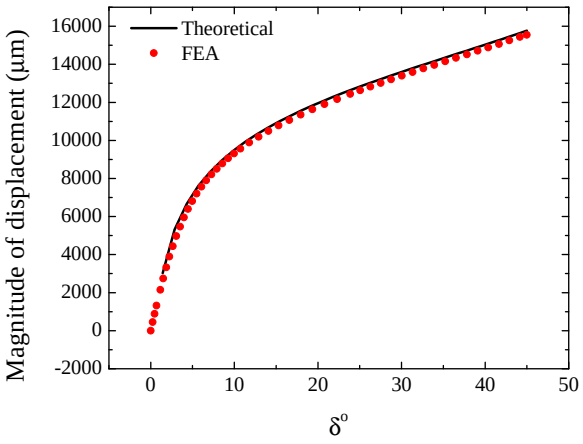

(c) $\vartheta = 30°$

Fig. 2 Comparison of theoretical and FEA results on magnitude of displacement, the composite lay-up of the antenna shell is $[\pm\vartheta/\mp\vartheta/core/\pm\vartheta/\mp\vartheta]$, the diameter of the antenna is $2m$, the focal length $f = 0.5m$, the temperature variation is uniform and $\Delta T = 200°$C.

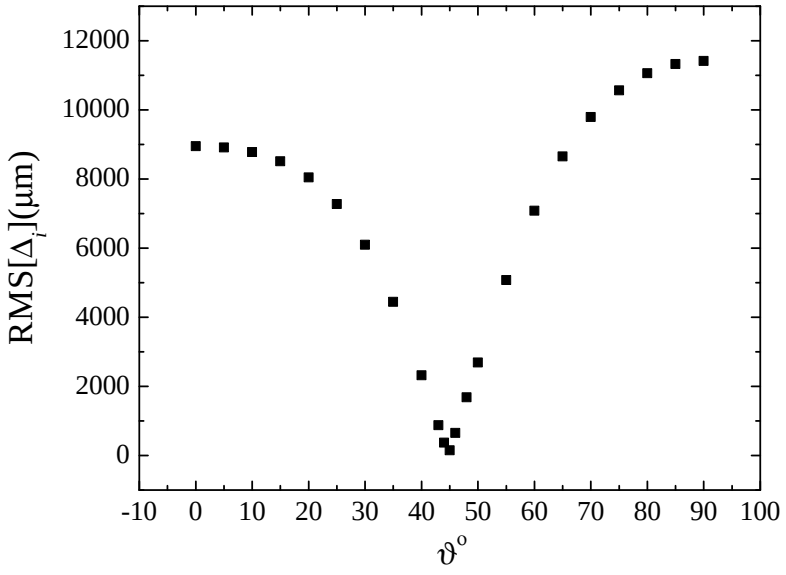

Fig. 3 RMS$[\Delta_i]$ of a paraboloid antenna with different ply-angle of the composite lay-up $[\pm\vartheta/\mp\vartheta/core/\pm\vartheta/\mp\vartheta]$, the diameter of the antenna is $2m$, the focal length $f = 0.5m$, $\Delta T = 200°$C.

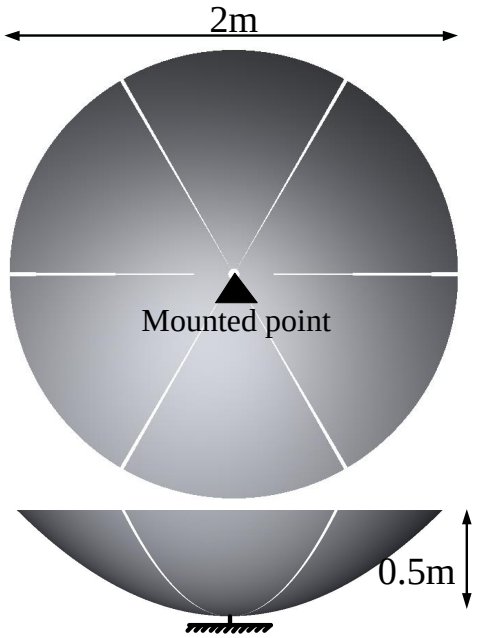

Fig. 4 A segmented paraboloid antenna reflector, the antenna reflector is segmented into 6 pieces, uniformly.

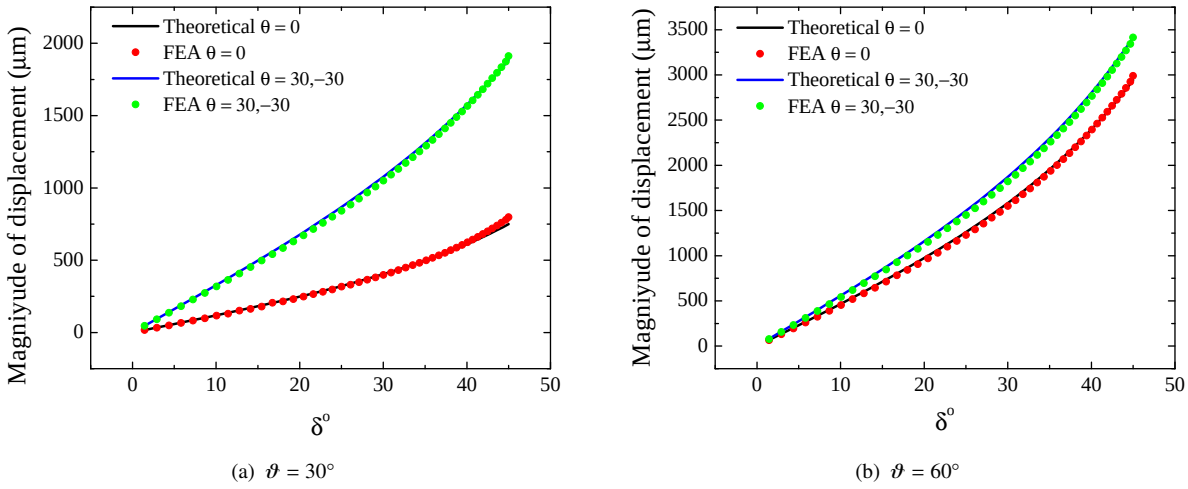

Fig. 5 Comparisons between theoretical prediction and FEA simulation results on the magnitudes of displacement fields for one piece of the segmented antenna reflector as shown in Fig. 4. The composite lay-up is $[\pm\vartheta/\mp\vartheta/core/\pm\vartheta/\mp\vartheta]$, the diameter of the antenna is $2m$, the focal length $f = 0.5m$, $\Delta T = 200°$C.

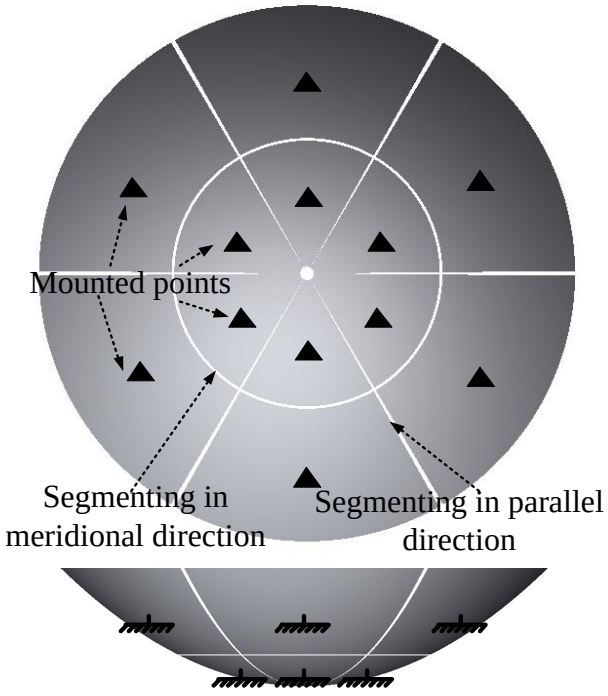

Fig. 6 A segmented paraboloid antenna reflector, the antenna reflector is segmented into 12 pieces (2×6)

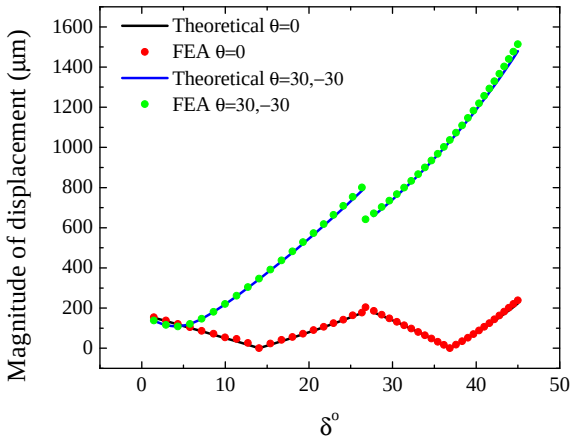

(a) $\vartheta = 30°$

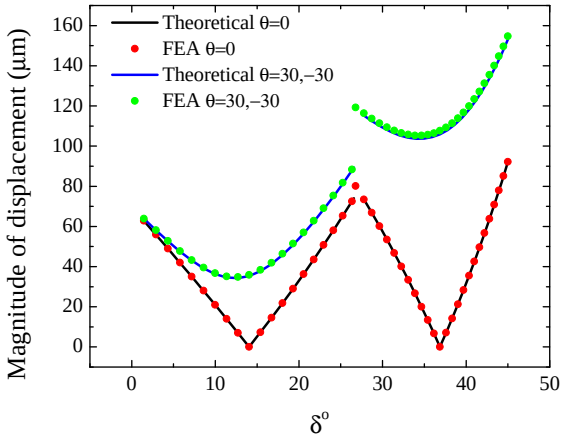

(b) $\vartheta = 45°$

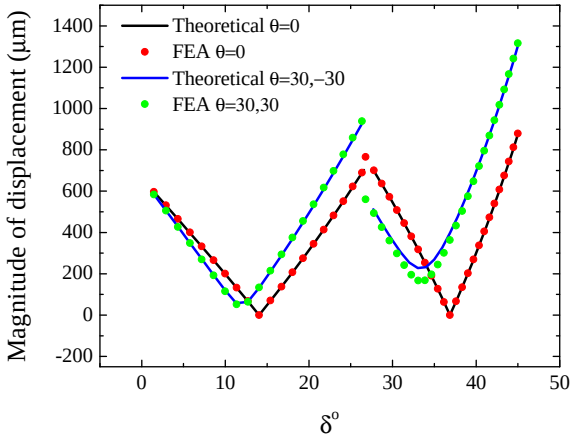

(c) $\vartheta = 60°$

Fig. 7 Comparisons between theoretical prediction and FEA simulation results on the magnitudes of displacement fields for one piece of the segmented antenna reflector as shown in Fig. 6. The composite lay-up is $[\pm\vartheta/\mp\vartheta/core/\pm\vartheta/\mp\vartheta]$, the diameter of the antenna is 2 m, the focal length $f = 0.5$ m, $\Delta T = 200°$C.

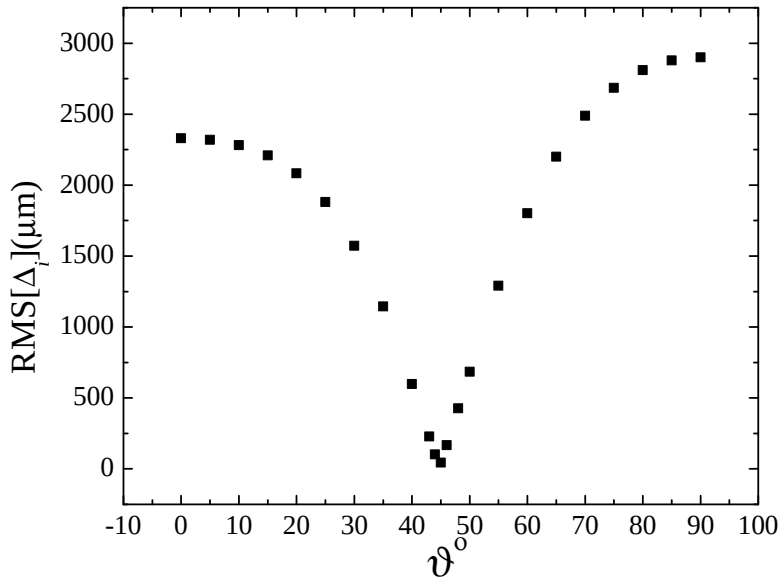

Fig. 8 RMS$[\Delta_i]$ of a segmented paraboloid antenna with 12 pieces predicted by theoretical model. The composite lay-up is $[\pm\vartheta/\mp\vartheta/core/\pm\vartheta/\mp\vartheta]$, the diameter of the antenna is 2 m, the focal length $f = 0.5$ m, $\Delta T = 200°$C.

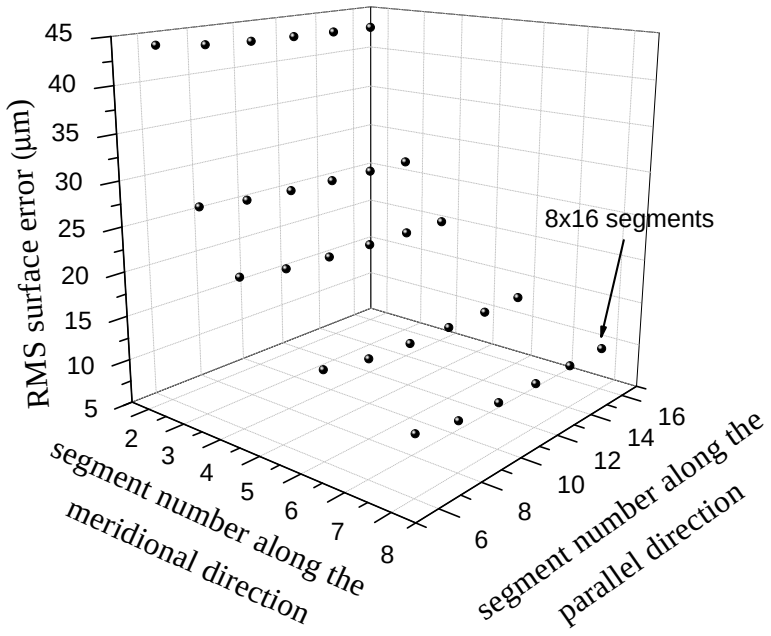

Fig. 9 Parametric study on the effects of the number of segments on the RMS surface error. The lay-up is $[\pm45/\mp45/core/\pm45/\mp45]$, the diameter of the antenna is 2 m, the focal length $f = 0.5$ m, $\Delta T = 200°$C

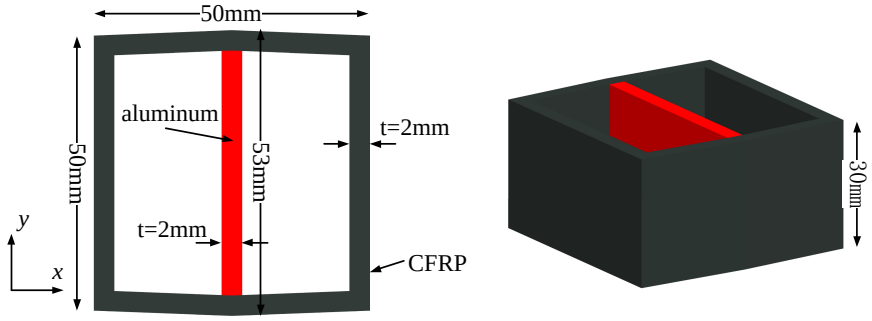

Fig. 10 A symmetric hexagon cell in the Thermally Stable Composite Structure.

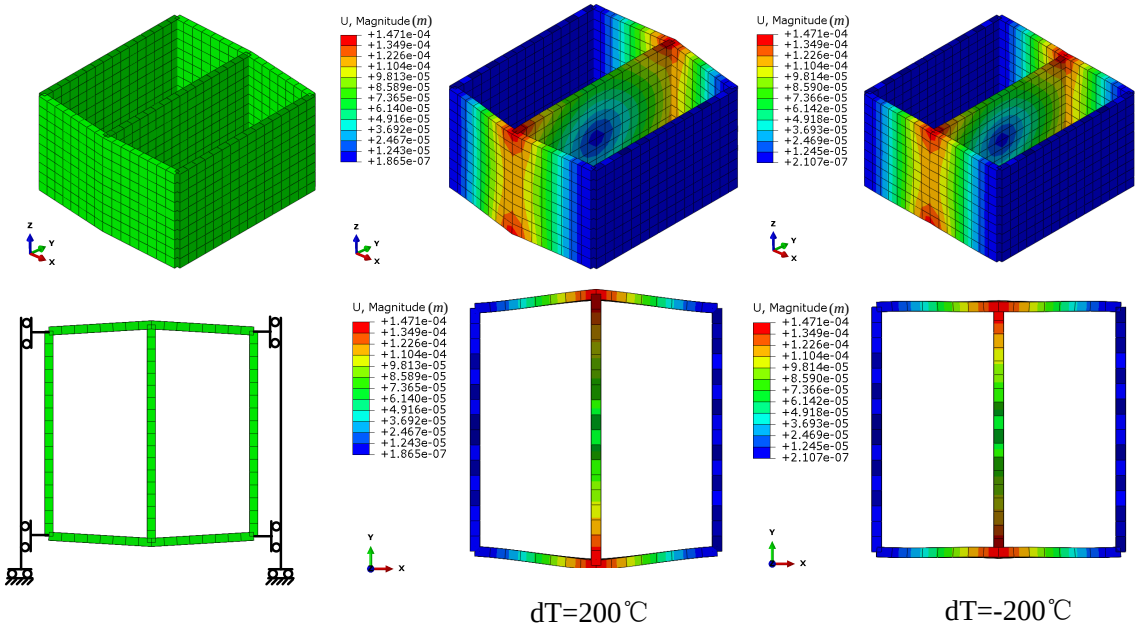

Fig. 11 Predicted thermal deformation of a cell of TSGS with symmetric boundary conditions. The thermal deformation of the cell is 10 times scaled for presentation.

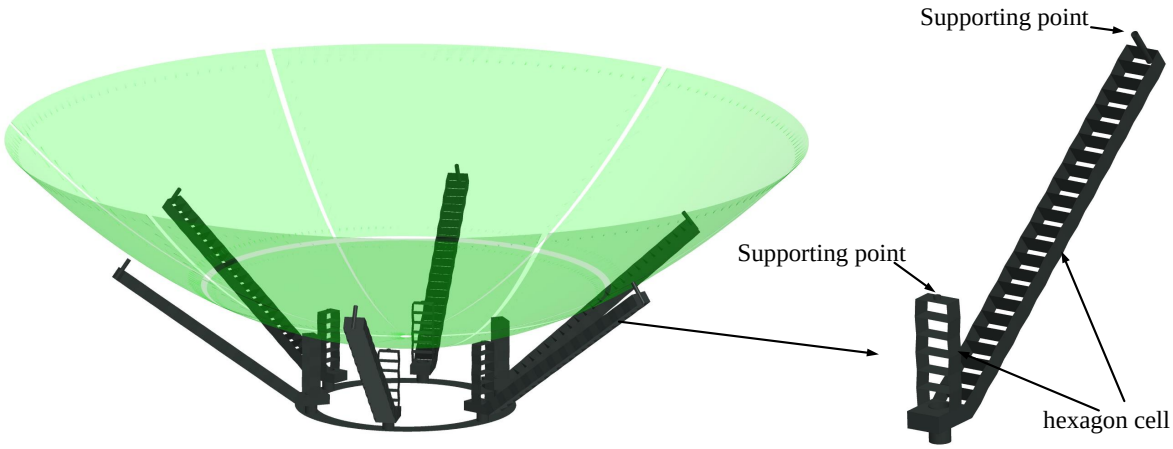

Fig. 12 An illustration of supporting thermally stable composite structure for a segmented antenna with 2×6 segments.

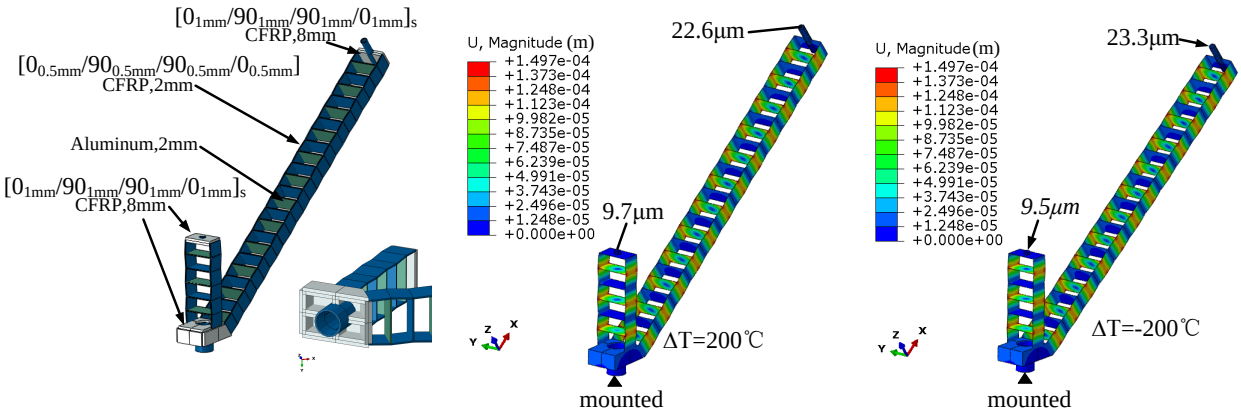

Fig. 13 Predicted thermal deformation of a TSGS, $\Delta T = \pm 200°$C.

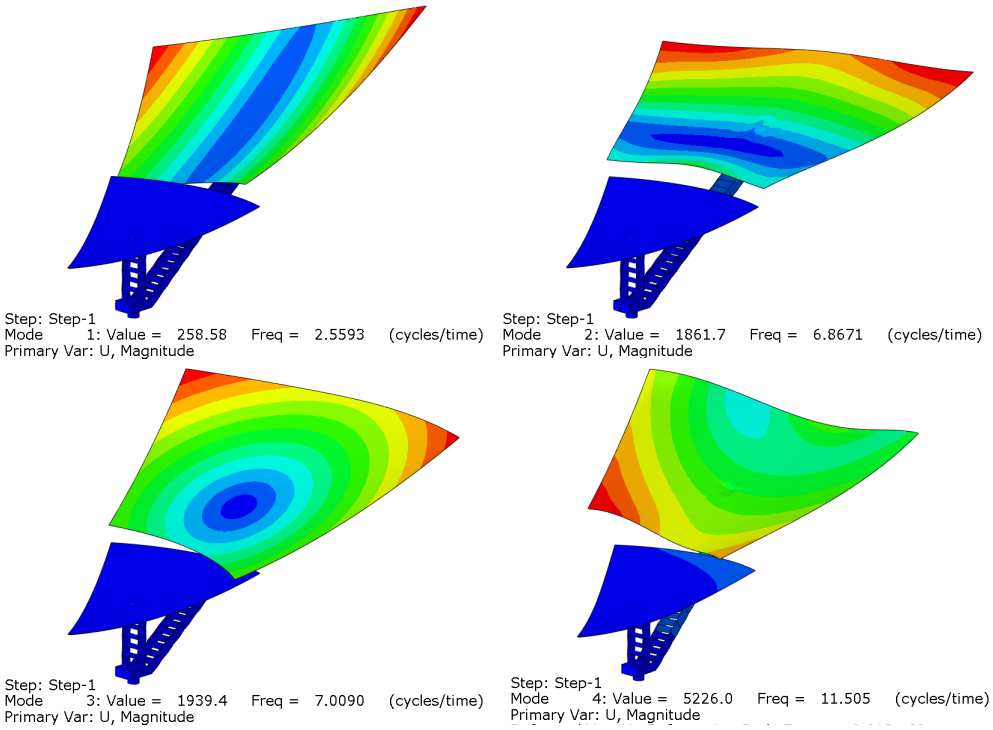

Fig. 14 Modal analysis of one-sixth of the segmented antenna.

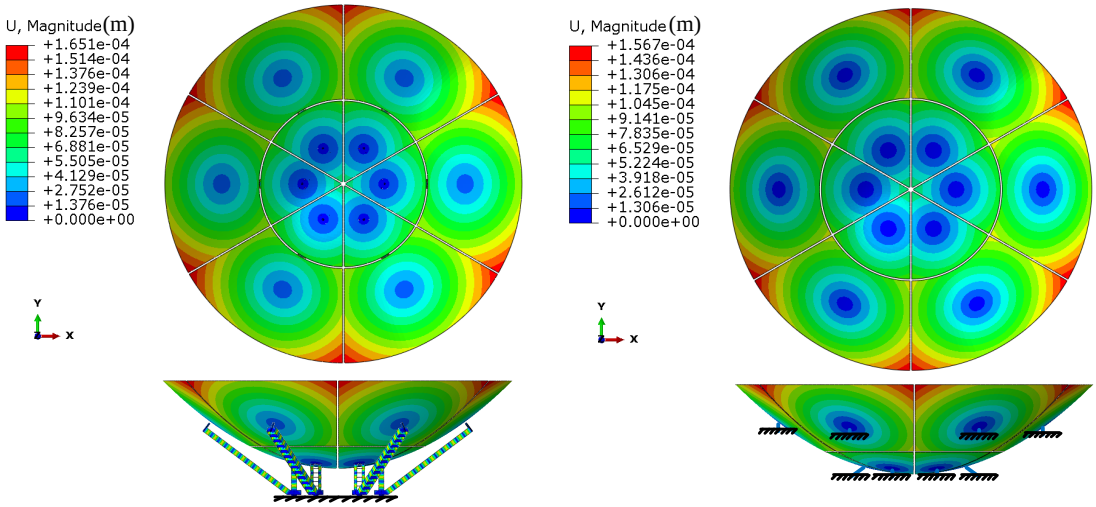

Fig. 15 Thermal deformation contour maps of a complete segmented antenna and a mounted antenna reflector. The lay-up is $[\pm 45/\mp 45/core/\pm 45/\mp 45]$, the diameter of the antenna is 2 m, the focal length $f = 0.5$ m, $\Delta T = 200^{\circ}$C.

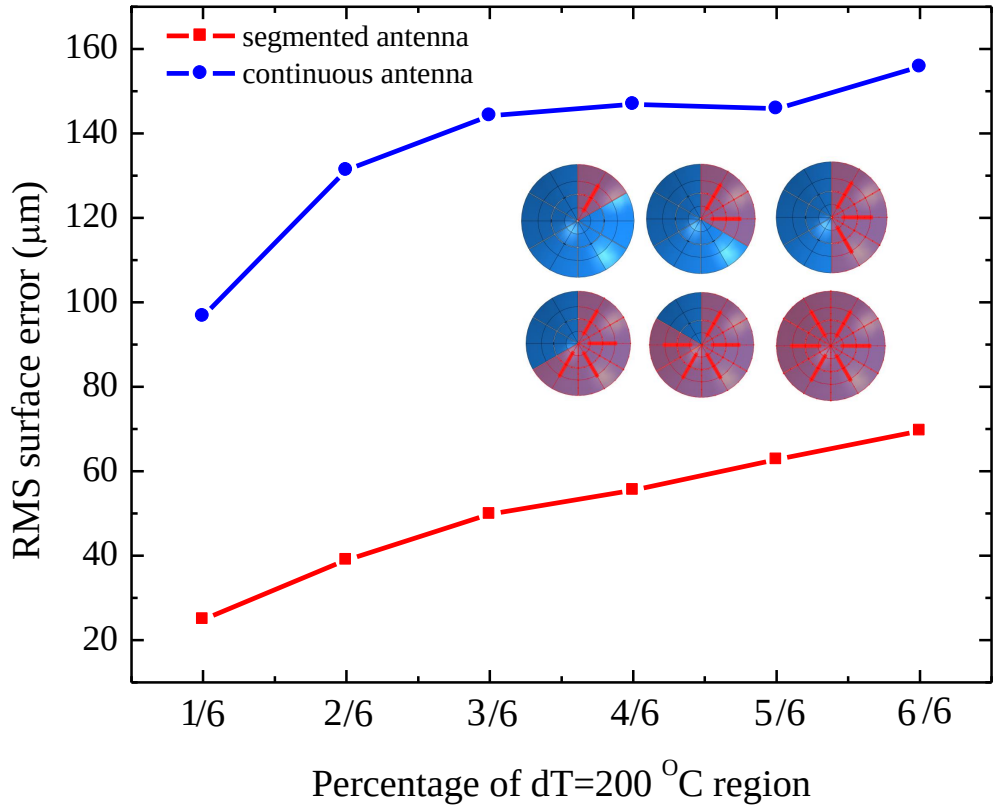

Fig. 16 A quantitatively analysis of the influence of non-uniform temperature variation on RMS surface error.

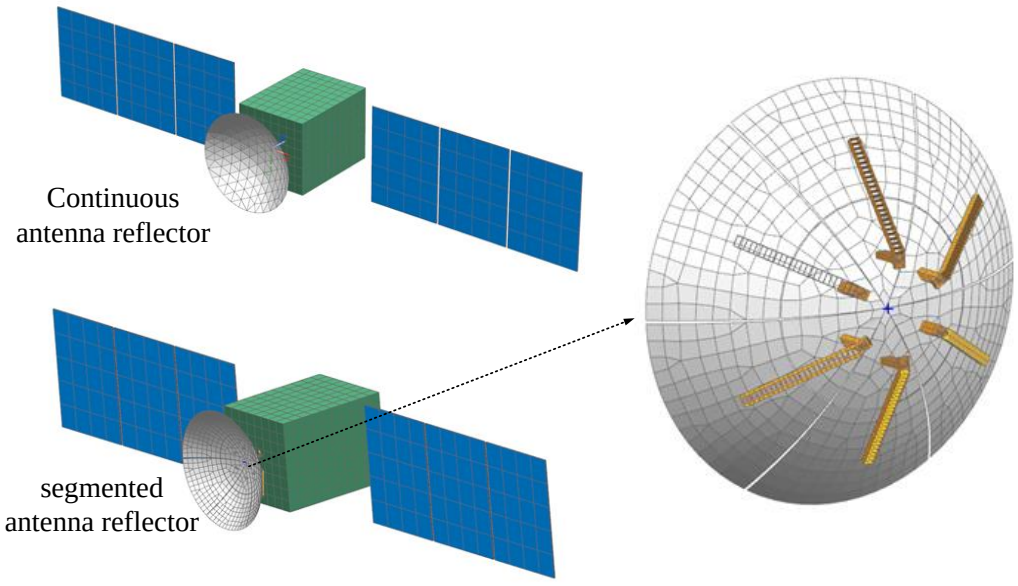

Fig. 17 An illustration of the thermal analysis model of the satellites with a segmented antenna and a continuous surface antenna.

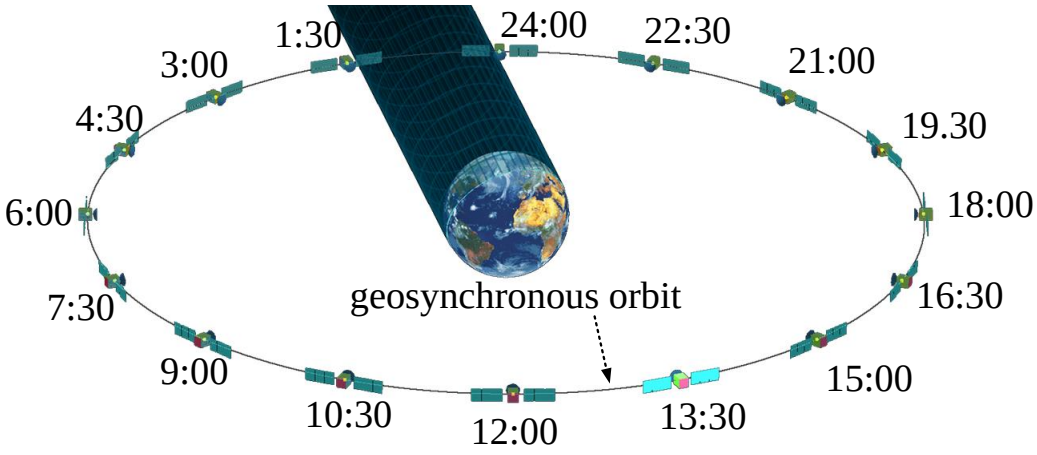

Fig. 18 Orbit setup of the cube satellite for thermal analysis.

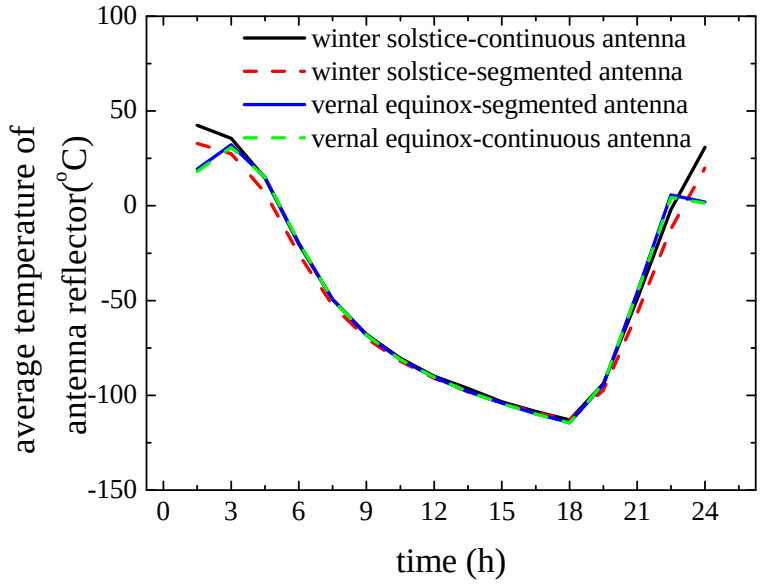

(a) Average temperature of the antenna reflector

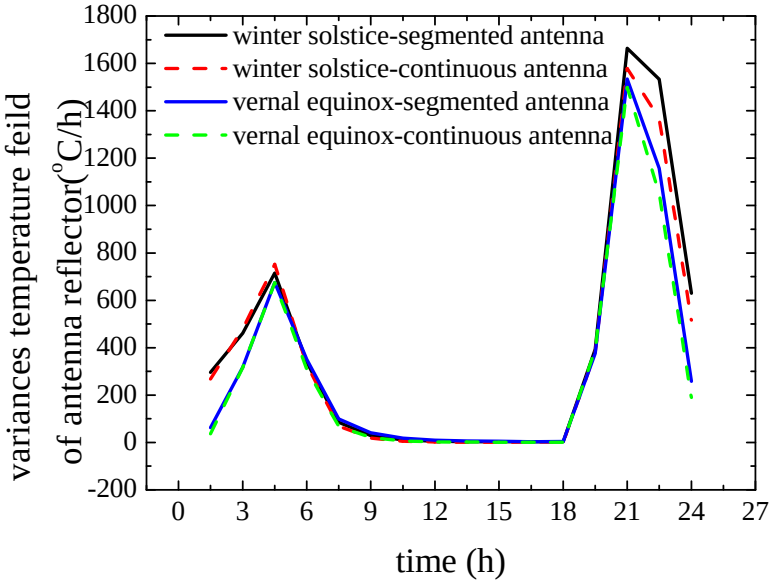

(b) Variance of the temperature of the antenna reflector

Fig. 19 Predicted average temperature and variance of the temperature of the antenna reflectors.

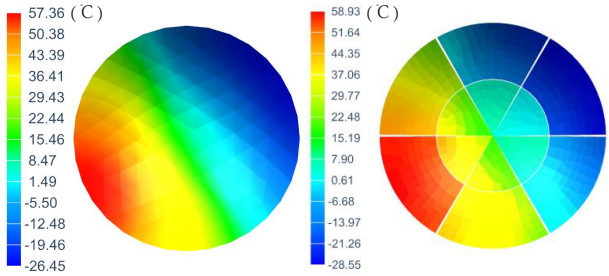

(a) Time=4:30

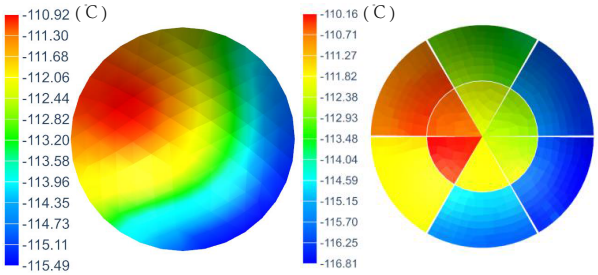

(b) Time=18:00

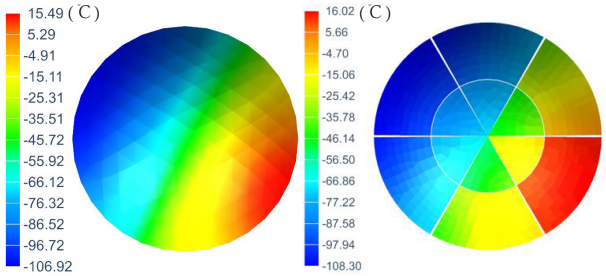

(c) Time=21:00

Fig. 20 Finite element analysis results of the temperature field of segmented and continuous surface antennas in geosynchronous orbit on winter solstice, predicted by NX [37].

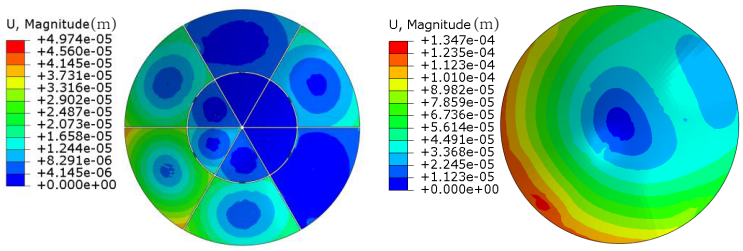

(a) Time=4:30

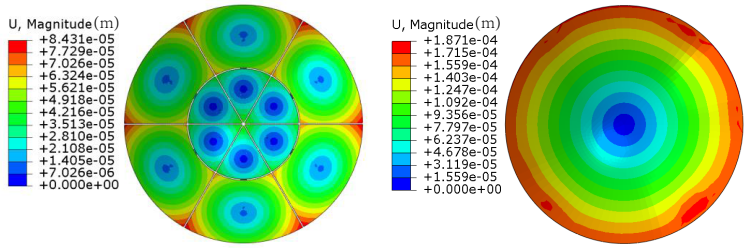

(b) Time=18:00

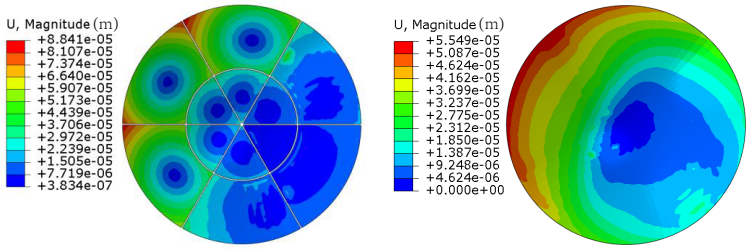

(c) Time=21:00

Fig. 21 Finite element analysis results of displacement magnitude contours of segmented and continuous surface antennas in geosynchronous orbit on winter solstice.

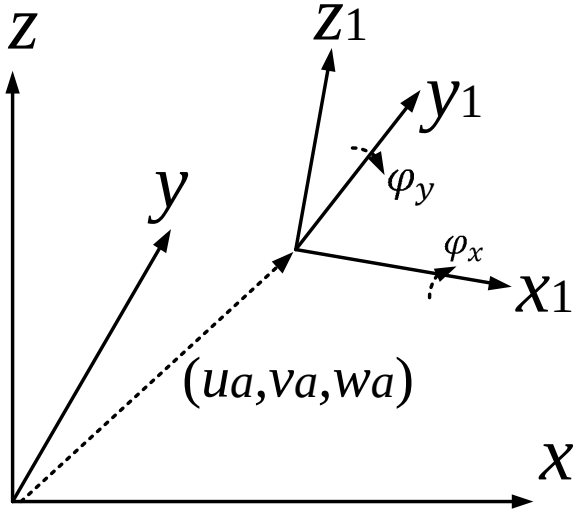

Fig. 22 The transition of Cartesian coordinate systems for the original and the fitted paraboloid surface.